

# Functional Mid-Infrared Polaritonics in van der Waals Crystals

Seyoon Kim, Sergey G. Menabde, Victor W. Brar,\* and Min Seok Jang\*

Despite high scientific and technological potential, nanophotonics research in the mid-infrared regime remains relatively less explored compared to other frequency bands, largely because the mid-infrared requires a totally different set of optical materials. Polaritons in layered 2D materials, or van der Waals (vdW) crystals, provide a new set of building blocks for mid-infrared nanophotonics. Herein, the recently reported polaritonic properties of various vdW crystals are summarized in the context of their mid-infrared applications. Both polaritons in vdW crystals with naturally anisotropic atomic structures as well as tunable plasmon polaritons in vdW semimetals are discussed. The extreme field confinement of 2D polaritons (confinement factors  $\approx 100$ ) enhances both their radiative heat transfer as well as the optical coupling to the vibrational modes of molecules, allowing for highly sensitive chemical detection. Their tunable properties, meanwhile, enable dynamic modulation of mid-infrared light to realize dynamic phase shifters, mid-infrared modulators, and spectrally tunable thermal emitters. By vertically stacking vdW crystals, it is possible to create a large variety of new effective materials with substantially different polaritonic properties compared to their building blocks.

## 1. Introduction

The mid-infrared region (2–20  $\mu\text{m}$ ) is not only scientifically interesting but also has high applicability. First, the earth's atmosphere is almost transparent in the 3–5 and 8–12  $\mu\text{m}$  wavelength range, called the infrared atmospheric windows. The mid-infrared thus can be used for medium- to long-range telecommunications and imaging even under cloudy conditions. Second, most molecules have their characteristic vibrational and rotational modes in the mid-infrared. By detecting these strong and unique spectral fingerprints from light–molecule interactions, it is possible to achieve efficient bioimaging and chemical sensing that overcomes the limitations of Raman

scattering-based chemical detection.<sup>[1,2]</sup> Third, the thermal radiation of objects with moderate temperatures (from room temperature to 1000 °C) peaks in the mid-infrared region. Therefore, by acquiring the ability to modulate the mid-infrared radiation of materials, it becomes possible to control the thermal emission properties of a heated object without altering its temperature.<sup>[3]</sup>

Even with these intriguing properties, the mid-infrared region has rather been less explored compared to other frequency regimes, because it requires a totally different set of materials for light sensing and control. In particular, the field of mid-infrared nanophotonics, which studies the behavior of light in subwavelength nanostructures, is still in its infancy, and the development of both the materials and the devices is essential. In this context, this progress report introduces layered 2D materials and their polaritonic properties

as a new set of functional building blocks for mid-infrared nanophotonics.

Polaritons are hybrid particles resulting from a strong coupling of photons with dipolar excitations such as atomic vibrations in polar dielectrics (phonon polaritons of mid-infrared energies), electron–hole pairs in semiconductors (exciton polaritons in materials with optical bandgap down to 0.4 eV), electron oscillations in metals (plasmon polaritons supported by different materials across a broad frequency range), and Cooper pairs in superconductors.<sup>[4,5]</sup> Among various types of polaritons, this progress report focuses on phonon polaritons and plasmon polaritons, which exist at mid-infrared frequencies. Polaritons in layered 2D materials, often referred to as van der Waals crystals, exhibit a few distinctive characteristics, providing an interesting and unique platform for mid-infrared nanophotonics. First, due to their structural anisotropy, van der Waals (vdW) crystals naturally show optical birefringence.<sup>[6,7]</sup> This opens up an interesting possibility to realize hyperbolic polaritons. Second, polaritons in 2D materials are often highly confined with low loss. By “squeezing” the electromagnetic waves into deeply subwavelength volumes, the polaritons in vdW crystals enable significantly enhanced light–matter interactions, which can overcome the limitations imposed by weak interactions in conventional materials. Third, the planar geometry and low carrier densities of 2D metals enable a dynamic tuning of their plasmon polariton properties via electrostatic gating, which unlocks the doorway to active nanophotonic devices.<sup>[8,9]</sup>

Dr. S. Kim, Prof. V. W. Brar  
Department of Physics  
University of Wisconsin-Madison  
Madison, WI 53706, USA  
E-mail: vbrar@wisc.edu

Dr. S. G. Menabde, Prof. M. S. Jang  
School of Electrical Engineering  
Korea Advanced Institute of Science and Technology  
Daejeon 34141, Korea  
E-mail: jang.minseok@kaist.ac.kr

 The ORCID identification number(s) for the author(s) of this article can be found under <https://doi.org/10.1002/adom.201901194>.

DOI: 10.1002/adom.201901194

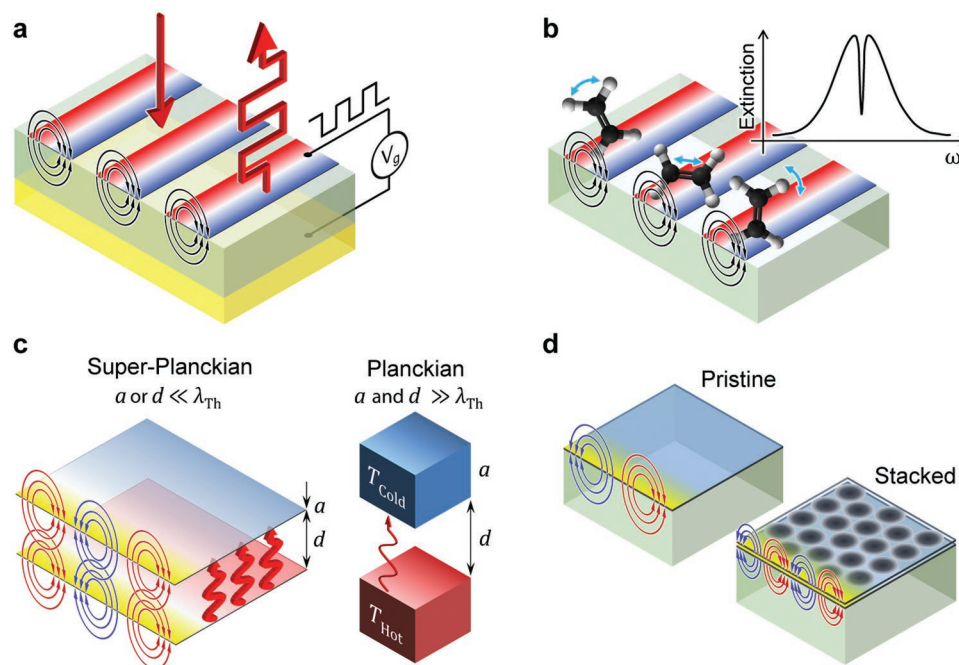


**Figure 1.** Diverse applications of mid-infrared polaritons in van der Waals crystals. a) Dynamic modulation of mid-infrared light: Electrical gating of 2D plasmonic materials changes their carrier concentration, allowing the active tuning of their electrodynamic response at mid-infrared frequencies. Dynamic modulation of emission, transmission, and reflection of mid-infrared light can be achieved by coupling the plasmon polaritons to desired photonic modes. b) Mid-infrared molecular sensing: strong field confinement of vdW polaritons enables efficient coupling with vibrational modes of molecules, most of which are in mid-infrared band. This interaction can be detected in far-field, providing the spectral information about the molecular species. c) Super-Planckian radiative heat transfer: Due to the deeply subwavelength and anisotropic nature of polaritons in vdW crystals, the radiative heat transfer between vdW materials can overcome the Planckian black body limit, which only holds in far-field macroscopic regime. d) Dispersion engineering of vdW polaritons: The dispersion of mid-infrared polaritons can be substantially manipulated by stacking vdW crystals and controlling their interlayer interaction via superlattice formation.

This progress report focuses on the mid-infrared applications of polaritons in vdW crystals with a special emphasis on highlighting the important breakthroughs in the last couple of years. In Section 2, we introduce the fundamental polaritonic properties of four representative vdW crystals: hexagonal boron nitride (h-BN), graphene, black phosphorous (BP), and  $\alpha$ -phase molybdenum trioxide ( $\alpha$ -MoO<sub>3</sub>), which was recently demonstrated to support ultralow loss, in-plane anisotropic hyperbolic phonon polaritons.<sup>[10–12]</sup> In Section 3, we discuss the recent developments in active mid-infrared optical modulation based on 2D plasmons (Figure 1a), including tunable perfect absorption in graphene employing multiscale metasurface architectures.<sup>[13]</sup> Section 4 discusses highly sensitive molecular detection schemes based on strong couplings between vdW polaritons and molecular vibrations, due to their extreme field confinement (Figure 1b) that can be squeezed down to a single-atom-thickness length scale.<sup>[14]</sup> Section 5 focuses on thermal emission engineering, one of the most important mid-infrared applications, and introduces dynamic modulation of thermal emission spectra<sup>[15]</sup> (Figure 1a) and strong radiative heat transfer between vdW crystals exceeding Planck's black body limit,<sup>[16]</sup> as schematically demonstrated in Figure 1c. Finally, in Section 6, we explore vast possibilities of engineering the dispersion of polaritons by creating new vdW heterostructures via stacking 2D materials vertically, as sketched in Figure 1d.

This includes recent breakthroughs in polaritonics based on moiré vdW superlattices.<sup>[17]</sup>

## 2. Anisotropic Polaritons in van der Waals Crystals

In this section, we discuss fundamental polaritonic properties of four representative vdW crystals. The first two materials, hexagonal boron nitride (h-BN) and  $\alpha$ -phase molybdenum trioxide ( $\alpha$ -MoO<sub>3</sub>), are insulators with optical phonons that support uniaxial (h-BN) and biaxial ( $\alpha$ -MoO<sub>3</sub>) anisotropic phonon polaritons in their reststrahlen bands. The second two, graphene and black phosphorous (BP), are semimetals, and possess plasmon polaritons whose properties are tunable by controlling their carrier concentrations. Plasmons in graphene are in-plane isotropic, while BP plasmons exhibit a strong anisotropy. The properties of polariton modes are characterized by their complex wavevector  $k_p$ . One important property is the confinement factor,  $n_{\text{eff}}$ , which is the ratio between the free space wavelength  $\lambda_0$  to the polariton wavelength  $\lambda_p$ , and can be derived by normalizing the real part of  $k_p$  to the free space wavevector  $k_0$  (i.e.,  $n_{\text{eff}} \equiv \text{Re}\{k_p\}/k_0$ ). Another useful parameter is the damping factor,  $\gamma \equiv \text{Im}\{k_p\}/\text{Re}\{k_p\}$ , which is defined such that  $\gamma^{-1}$  quantifies the number of wavelengths a polariton mode propagates until dissipation. The polaritons in vdW crystals are often highly confined ( $n_{\text{eff}} \approx 20$ <sup>[18,19]</sup>–300<sup>[14,20]</sup>) and long-lived ( $\gamma^{-1} \approx 10 - 200$ <sup>[11,18]</sup>).

**Table 1.** Experimentally obtained anisotropic optical properties of h-BN and  $\alpha$ -MoO<sub>3</sub>.

Material Direction	h-BN <sup>[18,99]</sup>		$\alpha$ -MoO <sub>3</sub> <sup>[10–12,160]</sup>		
	In-plane	Out-of-plane	In-plane		Out-of-plane
			[100]	[001]	[010]
$\epsilon_{\infty}$	4.9–4.98	2.95	4	5.2	2.4
$\omega_{\text{TO}}$ [cm <sup>-1</sup> ]	1360–1363	760	818–820	545	958–963
$\omega_{\text{LO}}$ [cm <sup>-1</sup> ]	1614–1617	825	963–974	851	1003–1010
$\Gamma$ [cm <sup>-1</sup> ]	7–7.3	3	4	4	2

## 2.1. Hyperbolic Phonon Polaritons in h-BN and $\alpha$ -MoO<sub>3</sub>

Artificial hyperbolic metamaterials—where nanofabrication methods are used to create a material with an anisotropic optical response—are a major field of study in the photonics community due to their ability to realize novel phenomena, such as negative refraction,<sup>[21,22]</sup> hyperlensing,<sup>[23,24]</sup> nonconventional quantum properties,<sup>[25]</sup> and anisotropic wave-guiding.<sup>[26]</sup> However, artificial metamaterials often suffer from substantial optical losses, while the difficulty of fabrication severely limits their practicality at optical frequencies. Recently, it was demonstrated that polar insulating van der Waals crystals can support natural hyperbolic phonon polaritons with exceptionally low losses and deep-subwavelength field confinement.<sup>[11,12,18,19]</sup>

The structural anisotropy of layered materials naturally creates different in-plane ( $\epsilon_{\parallel}$ ) and out-of-plane ( $\epsilon_{\perp}$ ) permittivities in van der Waals crystals. More generally, the frequency-dependent relative permittivity of a polar dielectric can be described by the Lorentz model as

$$\epsilon_j(\omega) = \epsilon_{\infty,j} \left( 1 + \frac{\omega_{\text{LO},j}^2 - \omega_{\text{TO},j}^2}{\omega_{\text{TO},j}^2 - \omega^2 - i\omega\Gamma_j} \right) \quad (1)$$

where the index  $j$  indicates the crystal orientation, and  $\omega_{\text{TO}}$ ,  $\omega_{\text{LO}}$ , and  $\Gamma$  are the transverse, longitudinal optical phonon frequencies, and the damping rate, respectively. We summarize the phononic properties of h-BN, the most widely investigated vdW polaritonic material, in **Table 1**.

h-BN is an insulator having a large bandgap ( $\approx 6$  eV) with its atomic structure composed of sp<sup>2</sup> hybridized alternating boron and nitrogen atoms constituting a honeycomb lattice (lattice constant 0.25 nm; single layer thickness 0.33 nm).<sup>[27]</sup> Due to its in-plane isotropy, h-BN exhibits uniaxial optical properties with a degenerate in-plane phonon mode at 1360 cm<sup>-1</sup> and an out-of-plane phonon at 760 cm<sup>-1</sup> in its naturally abundant form (**Figure 2a**).<sup>[18,28]</sup> In the two reststrahlen bands, the in- and out-of-plane permittivities of h-BN have opposite signs ( $\epsilon_{\parallel}\epsilon_{\perp} < 0$ ), and thus, the dispersion relations of both bands become hyperbolic,  $k_{\perp}^2/\epsilon_{\parallel} + k_{\parallel}^2/\epsilon_{\perp} = k_0^2$ , where  $k_{\parallel}$  and  $k_{\perp}$  are the in-plane and out-of-plane components of the wave-vector, respectively. The upper reststrahlen band with  $\epsilon_{\parallel} < 0$  and  $\epsilon_{\perp} > 0$  (Type II hyperbolicity) spans at  $\omega = 1370$ – $1610$  cm<sup>-1</sup>, while the lower band with reversed signs of permittivity components (Type I hyperbolicity) comprises  $\omega = 750$ – $820$  cm<sup>-1</sup>. The isofrequency curves for the two reststrahlen bands are shown on the right panel of **Figure 2a**. Notably, the curve slope has different signs for different bands, which is a consequence of the group velocity

vector pointing at opposite directions. In principle, these hyperbolic polariton modes can have arbitrarily large wave vectors and infinitely many transverse branches regardless of the material thickness.<sup>[19]</sup> The experimentally observed confinement factor of h-BN hyperbolic phonon polaritons reaches up to  $n_{\text{eff}} \approx 50$ .<sup>[11,18,28,29]</sup> Phonon polaritons exhibit relatively low losses compared to plasmon polaritons because their lifetime is not affected by the electronic losses, but mainly dictated by the crystal quality of the atomic lattice. The losses in natural h-BN crystals are demonstrated to be lower than that of most of the plasmonic materials ( $\gamma^{-1} \approx 15$ – $30$ ),<sup>[28,29]</sup> and can be further reduced through isotopic enrichment ( $\gamma^{-1} \approx 40$ ).<sup>[18]</sup>

As a natural next step, researchers have pursued polaritons with biaxial anisotropy, which requires a material exhibiting three different permittivities along different directions ( $\epsilon_x \neq \epsilon_y \neq \epsilon_z$ ). One way to achieve this condition is to periodically pattern a thin layer of uniaxial anisotropic material ( $\epsilon_x = \epsilon_y \neq \epsilon_z$ ) such as h-BN, such that it exhibits asymmetric in-plane effective permittivities.<sup>[30]</sup> Unlike h-BN,  $\alpha$ -MoO<sub>3</sub> naturally exhibits strong in-plane structural anisotropy due to the variations in the interlayer spacing for different crystal orientations (lattice constants are 0.396, 0.369, and 1.385 nm for  $x$  [100],  $y$  [001], and  $z$  [010] crystalline directions, respectively).<sup>[11]</sup> The broken symmetry imposes biaxial optical properties on  $\alpha$ -MoO<sub>3</sub> with three distinctive phonon modes at 820, 545, and 960 cm<sup>-1</sup> along  $x$ ,  $y$ , and  $z$  crystalline directions, respectively, as summarized in **Table 1**. Consequently, the in-plane dispersion of phonon polaritons in  $\alpha$ -MoO<sub>3</sub> is hyperbolic in the first (545 to 851 cm<sup>-1</sup>,  $\epsilon_x, \epsilon_z > 0$  and  $\epsilon_y < 0$ , Type II) and second (820 to 972 cm<sup>-1</sup>,  $\epsilon_y, \epsilon_z > 0$  and  $\epsilon_x < 0$ , Type II) reststrahlen bands, and elliptical in the third reststrahlen band (958 to 1010 cm<sup>-1</sup>,  $\epsilon_x \neq \epsilon_y > 0$  and  $\epsilon_z < 0$ , Type I),<sup>[12]</sup> as demonstrated in **Figure 2b**. Near-field imaging of phonon polaritons in  $\alpha$ -MoO<sub>3</sub> nanodisks allows direct measurement of their dispersion, demonstrating the elliptical and hyperbolic types at corresponding frequencies, as shown in **Figure 2c,d**.<sup>[11]</sup> Here, the near-field imaging was performed with a scattering-type scanning near-field optical microscope (s-SNOM),<sup>[31]</sup> where a nanotip effectively couples the far-field with the near-fields via inelastic scattering, overcoming the momentum mismatch and thus enabling the excitation and detection of polaritonic modes.<sup>[32]</sup> The confinement factor of  $\alpha$ -MoO<sub>3</sub> phonon polaritons is measured to be as high as  $n_{\text{eff}} \approx 60$ , and, surprisingly, the lifetime reaches up to 8 ps ( $\gamma^{-1} \approx 200$ ) which is about four times higher than that of the phonon polaritons in isotopically enriched h-BN.<sup>[11]</sup> The strong field confinement and ultralow loss of hyperbolic phonon

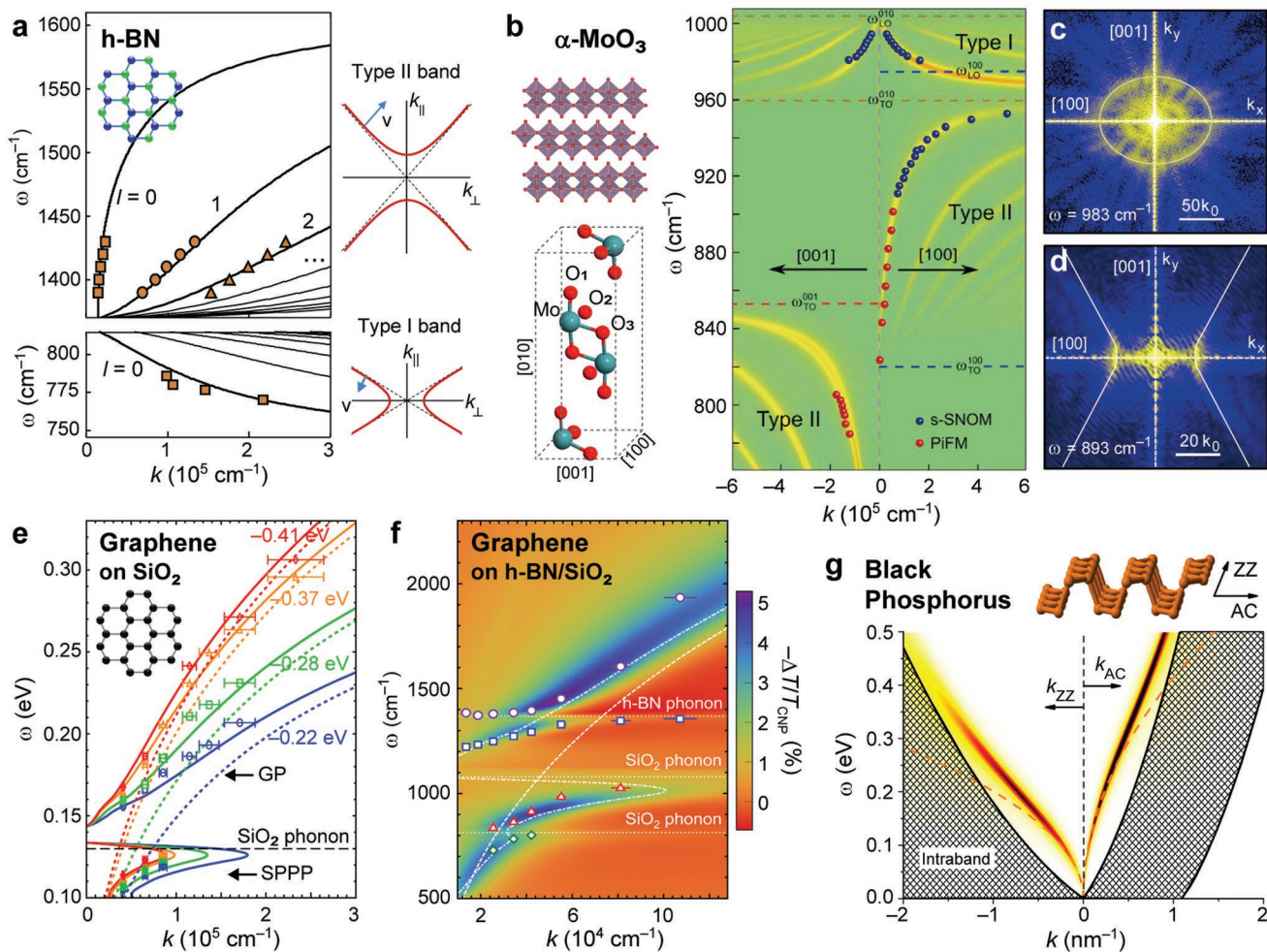


**Figure 2.** Dispersion of mid-infrared polaritonic species in the four representative 2D materials. a) Calculated (solid) and measured (data points) dispersion of phonon polaritons in 105 nm-thick stack of h-BN in the two reststrahlen bands; right panel: hyperbolic dispersion of h-BN phonons in the corresponding reststrahlen bands, with indicated group velocity vector (blue arrow). Adapted with permission.<sup>[28]</sup> Copyright 2015, Springer Nature. b) Left panel: orthorhombic lattice structure of layered  $\alpha$ -MoO<sub>3</sub> (top) and atomic structure of its unit cell (bottom). Adapted with permission.<sup>[11]</sup> Copyright 2018, Springer Nature. Right panel: calculated (imaginary part of the complex reflectivity; color map) and measured (red and blue data points) dispersion of hyperbolic phonons in the  $\alpha$ -MoO<sub>3</sub> flake on SiO<sub>2</sub> substrate. Adapted with permission.<sup>[12]</sup> Copyright 2019, AAAS. c,d) Fourier transform (absolute value) of the near-field images of the phonons at upper and lower reststrahlen bands, with fitted isofrequency contours. (c,d) Adapted with permission.<sup>[11]</sup> Copyright 2018, Springer Nature. e) Tunable dispersion of plasmon polaritons in graphene on a dispersionless substrate (calculated; dashed) and on SiO<sub>2</sub> (calculated/measured; solid curves/data points). Adapted with permission.<sup>[54]</sup> Copyright 2013, American Chemical Society. f) Calculated (color map) and experimental (data points) change in transmission for graphene/monolayer h-BN/SiO<sub>2</sub> nanoresonators of varying width at a carrier density of  $1 \times 10^{13} \text{ cm}^{-2}$ , normalized relative to zero carrier density; dashed and dotted-dashed lines indicate theoretical dispersion of plasmons in bare graphene and graphene on SiO<sub>2</sub>, respectively. Adapted with permission.<sup>[100]</sup> Copyright 2014, American Chemical Society. g) Loss function,  $-\text{Im}[1/\epsilon(k, \omega)]$ , calculated for monolayer BP for  $k$  along the two crystal axes, as indicated in the inset;  $n^{2D} = 1 \times 10^{13} \text{ cm}^{-2}$ ,  $\Gamma = 10 \text{ meV}$ ,  $T = 300 \text{ K}$ . Shaded regions denote the Landau damping regions. Adapted with permission.<sup>[46]</sup> Copyright 2014, American Physical Society.

polaritons in h-BN and  $\alpha$ -MoO<sub>3</sub> provide a new and interesting physical platform with strong and directional light–matter interaction, enabling the realization of nanoscale photonic devices for a range of applications from deeply subdiffractional imaging<sup>[28,30]</sup> to molecular spectroscopy.<sup>[33]</sup>

## 2.2. Tunable Plasmons in Graphene and Black Phosphorous

Graphene and black phosphorus support plasmon polaritons from THz to mid-infrared frequencies. In the case of graphene,

the symmetry of the honeycomb lattice composed of carbon atoms imposes (for small  $k$ -vectors) an in-plane isotropy to the optical properties of graphene. When the Fermi energy of graphene is sufficiently higher than the electron temperature,  $|E_F| \gg k_b T$ , the in-plane isotropic sheet conductivity of monolayer graphene takes the following form within the local random phase approximation<sup>[34]</sup>

$$\sigma^{2D}(\omega, E_F) = \frac{ie^2|E_F|}{\pi\hbar^2(\omega + i\Gamma)} + \frac{e^2}{4\hbar} \left[ \theta(\hbar\omega - 2|E_F|) - \frac{i}{2\pi} \ln \frac{(\hbar\omega + 2|E_F|)^2}{(\hbar\omega - 2|E_F|)^2} \right] \quad (2)$$

**Table 2.** Effective mass of free carriers in bulk and single layer BP. AC and ZZ represent the armchair and zigzag crystal direction, respectively.

Carrier type		Electron			Hole		
Direction		AC	ZZ	⊥	AC	ZZ	⊥
Bulk	Experiment <sup>[161]</sup>	0.083	1.027	0.128	0.076	0.648	0.280
	Theory <sup>[162]</sup>	0.115	1.855	0.115	0.104	0.774	0.158
Single layer	Theory <sup>[44]</sup>	0.166	0.846	–	0.182	1.140	–

where  $e$  and  $\theta$  are the elementary charge and the step function, respectively.  $\Gamma$  is the carrier damping rate determined by impurities, defects, and electron–phonon scattering processes in graphene.<sup>[35]</sup> The Fermi level in graphene can be controlled by external doping,<sup>[8]</sup> with the resulting 2D carrier concentration given by  $n^{2D} = E_F^2 / (\pi \hbar^2 v_F^2)$ , where  $v_F = 10^6 \text{ m s}^{-1}$  is the Fermi velocity of free carriers in graphene.<sup>[36]</sup> The first term in Equation (2) originates from intraband electro-photon scattering processes and coincides with the Drude model, and the second term takes into account interband electron transitions. When graphene is doped enough to prompt Pauli blocking (i.e.,  $2|E_F| > \hbar\omega$ ), it supports low-loss plasmon polaritons. In the quasi-static limit ( $n_{\text{eff}} \gg 1$ ), the wavevector of graphene plasmons can be approximately derived as  $k_p \approx 2i \epsilon_0 \langle \epsilon \rangle \omega / \sigma^{2D}(\omega, E_F)$ , where  $\langle \epsilon \rangle$  is the average relative permittivity of the environment.<sup>[37]</sup> The dispersion of graphene plasmon polaritons is shown in Figure 2e,f demonstrating modes of graphene on both a dispersionless substrate (dashed) and SiO<sub>2</sub> substrate (solid), where in the latter case, graphene plasmons hybridize with SiO<sub>2</sub> phonons (as will be further discussed in Section 3.2). The confinement factor of graphene plasmons is largely dependent on both  $\omega$  and  $E_F$ ;  $n_{\text{eff}}$  increases with decreasing  $|E_F|$ , and has been experimentally shown to be as high as  $\approx 100$ , however, when  $|E_F|$  is too low, graphene plasmons are highly damped by interband transitions. The loss of graphene plasmon polaritons critically depends on the quality of the graphene sample and measurement condition. Large-area graphene grown by chemical vapor deposition (CVD) typically have  $\gamma^{-1} \approx 5$  or even less at room temperatures.<sup>[38,39]</sup> When a high-quality exfoliated graphene is encapsulated by h-BN,  $\gamma^{-1}$  can be as high as 25.<sup>[40]</sup> Recent experiment at low temperatures around  $T \approx 60 \text{ K}$  reports  $\gamma^{-1} \approx 130$ , which corresponds to the plasmon propagation length exceeding  $10 \mu\text{m}$ .<sup>[41]</sup>

BP is an emerging mid-infrared *biaxial* plasmonic van der Waals crystal. Similar to graphene, a single layer of BP has a honeycomb lattice, but its surface is puckered due to  $sp^3$  hybridization. These atomic corrugations induce strong in-plane anisotropy of the material properties along two distinct directions: the direction of atomic puckering (“armchair”; AC), and the direction perpendicular to it (“zigzag”; ZZ). The out-of-plane lattice constant is  $1.07 \text{ nm}$ .<sup>[42,43]</sup> Therefore, the optical conductivity of BP is different along each of the three crystal axes ( $\sigma_{AC} \neq \sigma_{ZZ} \neq \sigma_{\perp}$ ). Below the bandgap of BP, which ranges from 0.3 (bulk) to 2 eV (monolayer) depending on the number of layers,<sup>[44]</sup> the intraband bulk optical conductivity of BP can be approximated by using the Drude model

$$\sigma_j(\omega) = \frac{iD_j}{\pi(\omega + i\Gamma_j)} = \frac{ie^2n}{m_j(\omega + i\Gamma_j)} \quad (3)$$

where  $\Gamma$ ,  $D = \pi e^2 n / m_j$ ,  $e$ , and  $n$  are the damping rate, the Drude weight, the elementary charge, and the carrier concentration which is tunable via doping. The effective carrier mass,  $m_j$ , along each crystal direction is summarized in Table 2. The relative permittivity tensor  $\epsilon(\omega)$  relates to  $\sigma_j(\omega)$  as  $\epsilon_j = 1 + i\sigma_j/\epsilon_0\omega$ . In case of the monolayer BP, its permittivity can be obtained using the effective bulk conductivity  $\sigma_j(\omega) = \sigma_j^{2D}(\omega)/a$ , where  $a = 0.54 \text{ nm}$  is the thickness of a single BP layer.<sup>[42]</sup> Due to the strong biaxial anisotropy, the plasmon polaritons in BP (Figure 2g) are expected to show three different types of dispersion characteristics:<sup>[45,46]</sup> elliptic (permittivity tensor with metallic principal components of different magnitude), interband-induced quasi-isotropic (symmetric permittivity tensor), and hyperbolic (one of the principal components of the permittivity tensor is metallic and another is dielectric). Furthermore, the dispersion and type of anisotropy of these plasmons can be controlled via electrostatic doping and/or periodic patterning of the BP sheet.<sup>[45–48]</sup> Due to this tunability, BP may become an alternative to graphene as a 2D plasmonic material, while providing an anisotropic functionality. Plasmons in BP are extremely confined,  $n_{\text{eff}} \approx 10\text{--}10^3$ , and the confinement factor depends on both the frequency and the carrier density of BP.<sup>[4]</sup> To the best of our knowledge, to date, the direct observation of plasmon polaritons in BP has not been reported, and thus it is early to mention anything decisive on the lifetime of BP plasmons. The quantum oscillation measurements estimate the carrier lifetime of BP to be about 0.1 ps for both carrier types at cryogenic temperatures,<sup>[49]</sup> which corresponds to the mobility of  $500 \text{ cm}^2 \text{ V}^{-1} \text{ s}^{-1}$  and  $\gamma^{-1} \approx 1\text{--}10$ . One experimental work reported observation of interface polaritons, where plasmons in BP and phonons in SiO<sub>2</sub> are hybridized, and the measured lifetime of the hybrid interface phonon was  $\approx 5 \text{ ps}$ .<sup>[50]</sup>

### 3. Dynamic Light Modulation with Tunable Plasmons

As discussed in Section 2.2, the optical properties of plasmon polaritons in vdW crystals are largely tunable by adjusting the material carrier densities. Their atomically thin geometry, meanwhile, is ideal for creating structures that can be electrostatically gated. These two properties make vdW materials an effective and compact platform for active modulation of both guided waves<sup>[51,52]</sup> and free space light<sup>[53–55]</sup> at mid-infrared frequencies. The extremely confined nature of vdW plasmons, however, makes them difficult to couple strongly to the free waves and thus hinders their efficiency in optoelectronic devices.<sup>[56]</sup> Recent advances have shown that this wavevector mismatch problem can be overcome by introducing multiscale nanophotonic design, which enables electronically tunable perfect absorption in graphene.<sup>[13]</sup>

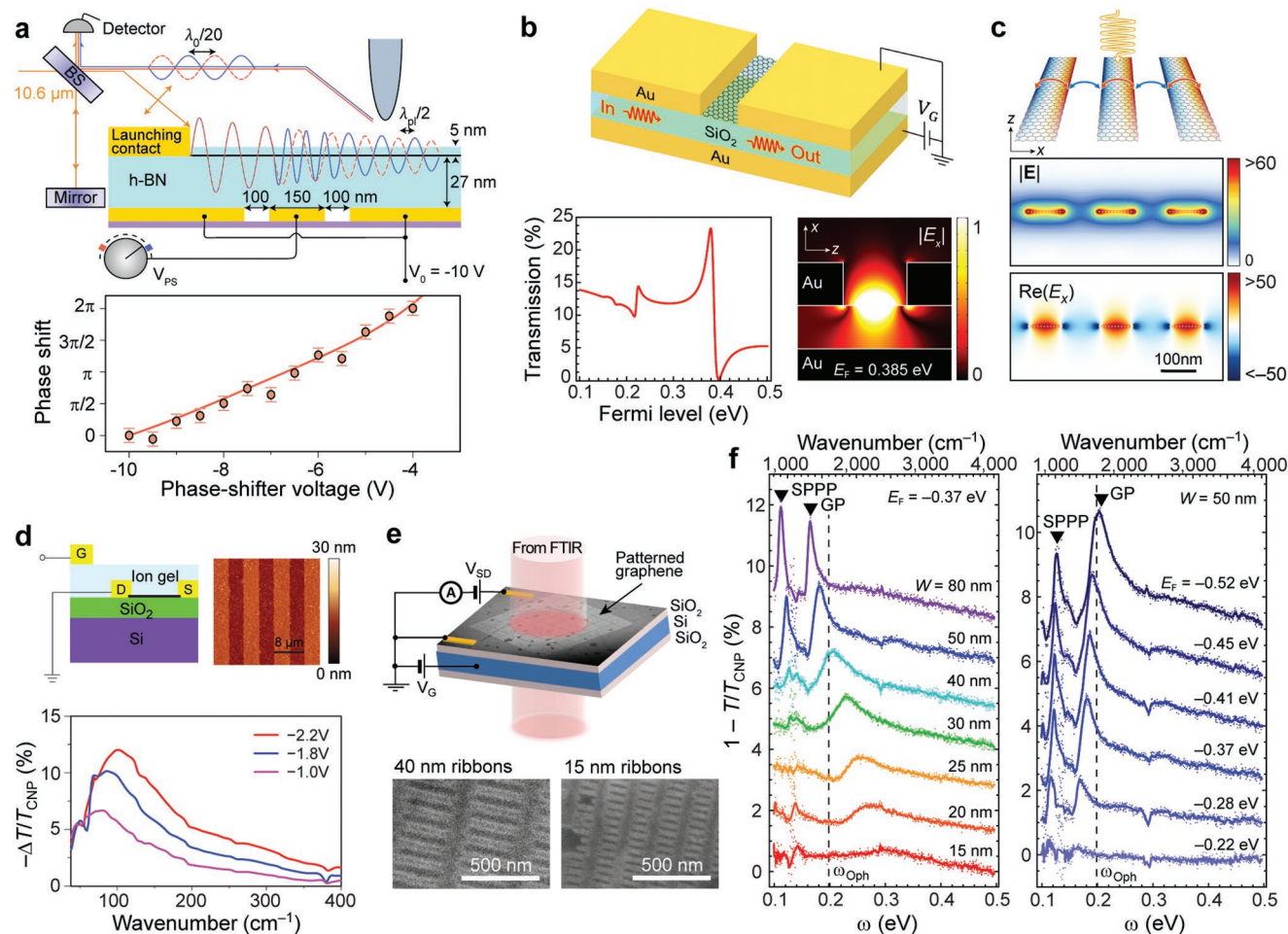


**Figure 3.** a) (Top) Electrical  $2\pi$  phase shift of graphene plasmons controlled by local phase-shifter voltage ( $V_{PS}$ ). (Bottom) Measured phase shift (orange circles) and calculated phase shift (orange curve). Adapted with permission.<sup>[51]</sup> Copyright 2017, Springer Nature. b) (Top) Schematic of resonant transmission modulation through a deep-subwavelength graphene plasmonic gap. (Bottom left) Calculated gate-dependent transmission across the gap. (Bottom right)  $|E_x|$  distribution around the gap with graphene plasmonic resonance at  $E_F = 0.385$  eV. Adapted with permission.<sup>[52]</sup> Copyright 2018, American Physical Society. c) (Top) Illustration of graphene nanoresonators supporting localized graphene plasmons with TM polarized incoming light. Red arrows and blue arrows represent graphene plasmons and intercoupling in the nanoresonators, respectively. (Middle)  $|E|$  distribution and (bottom)  $\text{Re}(E_x)$  distribution displaying large field enhancement by graphene plasmons. The dashed white lines correspond to graphene nanoresonators. d) (Top left) Schematic of graphene doping with ionic gel. (Top right) AFM image of patterned graphene microribbons. The ribbon width and the gap width are both 4  $\mu\text{m}$ . (Bottom) Measured gate-dependent THz light modulation. Adapted with permission.<sup>[66]</sup> Copyright 2011, Springer Nature. e) (Top) Graphene nanoresonators with capacitor-like electrostatic gating. (Bottom) SEM images of patterned graphene nanoribbons. The gap width is equal to the ribbon width. f) Measured mid-infrared light modulation (left) as varying the ribbon width and (right) as varying the doping level. (e,f) Adapted with permission.<sup>[54]</sup> Copyright 2013, American Chemical Society.

### 3.1. Modulation of Guided Waves

Graphene has been widely exploited to electronically modulate guided waves based on its tunable absorption and refractive index change, enabling broadband and ultrafast modulation.<sup>[57–60]</sup> In particular, the tunable and ultrahigh-confined properties of graphene plasmons discussed in Section 2.2 allow dynamic manipulation of electromagnetic waves at deep-subwavelength scale. For example, an in situ electrical  $2\pi$  phase shift has been experimentally demonstrated in graphene.<sup>[51]</sup> As shown in **Figure 3a**, propagating plasmons along encapsulated graphene were launched by a top metal contact, and their phase velocity, or the dispersion, was actively controlled by local gating. Surprisingly, the optical path length of the graphene

plasmons was observed to be tuned in the order of micrometers within a couple of hundreds nanometer length scale due to the ultrahigh confinement factor ( $n_{\text{eff}} \approx 100$ ). As a result of the modulated optical path lengths of the graphene plasmons, a dynamic  $2\pi$  phase shift was achieved within a  $\lambda_0/30$  length scale, which corresponds to 350 nm.<sup>[51]</sup>

In addition to the phase modulation in waveguides, graphene plasmons have been theoretically explored as a means of regulating mid-infrared transmission in noble metal plasmonic waveguides across a  $\lambda_0/50$  gap.<sup>[52]</sup> In that study, two metal–insulator–metal (MIM) waveguides were connected by a narrow junction covered by graphene, as shown in **Figure 3b**. In this structure, light transmission across the junction can be achieved through two optical pathways: background transmission modes

and graphene plasmons. Surface plasmons bound on the bottom gold layer and the unbound eigenmodes inside the gap correspond to the background transmission modes. These two components correspond to the background transmission mode, and their electromagnetic behaviors barely depend on the existence of graphene. In contrast to the background transmission modes, transmission through the graphene is determined by the graphene plasmonic resonance condition inside the gap. As a result, these two transmission modes interfere constructively or destructively depending on the graphene Fermi level, creating a Fano resonance, as shown in Figure 3b. Here, the resonant transmission could be totally suppressed by a complete destructive interference between the two modes.<sup>[52]</sup> In addition, the complete switching of the transmission could be achieved by a very small change in the graphene Fermi level (15 meV) owing to the sharp asymmetric line shape of the Fano resonance.

### 3.2. Free Space Light Modulation

While waveguide geometries naturally allow for strong interactions between vdW plasmons and light, free space modulation is also possible, and is generally more useful for optoelectronic applications. Figure 3c illustrates the basic schematic of light modulation using graphene nanoresonators with TM polarized incoming light. When the carrier density is varied, the plasmonic resonance condition for a particular nanoresonator width changes as the excited plasmons form standing wave-like localized modes. Similar to noble metal plasmonic nanoparticles or antennas, this plasmonic resonance in the patterned graphene results in resonant absorption at a specific frequency, allowing for direct interaction with free space photons. These types of light modulators are distinguished from other graphene-based light modulators in that graphene serves as an active plasmonic medium instead of tuning the local resonance environment of incorporated noble metal plasmonic structures.<sup>[61–65]</sup>

Light–matter interactions in patterned graphene nanoresonators have been experimentally demonstrated from THz to mid-infrared ranges. Ju et al. first demonstrated active THz light modulation in graphene ribbon array fabricated on SiO<sub>2</sub>/Si substrate, as shown in Figure 3d.<sup>[66]</sup> In this device, a CVD-grown graphene was patterned at 1 μm length scales using optical lithography, and ionic gels were used to control the graphene carrier density. In later experiments presented in Figure 3e, electron beam lithography was used to pattern CVD graphene down to 15 nm length scales in devices operating at mid-infrared frequencies.<sup>[54,67]</sup> In those types of experiments, the resonant frequency was tuned by two factors: the size of the graphene ribbons and the doping level of graphene. Equation (2) presented in Section 2.2 implies that, when  $|E_F| \gg 2\hbar\omega \gg k_b T$  and the dispersion of the substrate is negligible, the conductivity of graphene can be accurately described solely by the Drude-like intraband conductivity. These results at the resonant frequency that is approximately proportional to  $\sqrt{E_F}/\sqrt{W}$ , or  $n^{1/4}/\sqrt{W}$ , where  $W$  and  $n$  are the width of the graphene ribbon and the graphene carrier density, respectively, as shown experimentally in Figure 3f.<sup>[54,66,67]</sup> This dependency indicates that narrower patterns and higher doping are required to induce

plasmon resonances at higher frequencies. In particular, the doping level in Figure 3e was controlled by capacitor-like electrostatic gating, which is preferable over the use of ionic gels,<sup>[66,68,69]</sup> photodoping,<sup>[70]</sup> or chemical doping<sup>[67,71]</sup> for high-speed modulation and functional integration.

In addition to the tunable graphene plasmonic cavity modes (GP), other resonant peaks were observed in graphene nanoribbon transmission experiments, as can be seen in Figure 3f below 900 cm<sup>-1</sup> ( $\lambda_0 = 11.1 \mu\text{m}$ ).<sup>[54]</sup> Those resonances originate from surface plasmon phonon polaritons (SPPPs), which is a coupled mode between graphene plasmons and optical phonons in the SiO<sub>2</sub> layer.<sup>[72]</sup> Compared with graphene plasmons, these SPPPs were found to exhibit less dependency on the doping level and bound around the SiO<sub>2</sub> phonon energy. The strength of the SPPP resonance decreases with decreasing ribbon width, because the SPPP mode becomes lossier as its frequency approaches to the SiO<sub>2</sub> phonon energy.

Additional plasmonic modes in graphene devices have also appeared in high magnetic fields at THz frequencies due to the splitting of edge and bulk plasmons in graphene nanodisks.<sup>[73]</sup> Furthermore, in graphene nanorings, bonding and antibonding hybridized plasmons have been demonstrated, and resonant extinction close to near-infrared was achieved with the antibonding modes.<sup>[69]</sup> In addition to the graphene nanoresonators, some theoretical works have reported that far-infrared to THz light modulation could be achievable with nanostructured monolayer black phosphorus, which also supports highly confined localized plasmons modes.<sup>[47,74,75]</sup>

### 3.3. Major Obstacles in Strong Light Modulation

In the electrostatic modulator experiments described before, the resonant modulation efficiency was relatively low in contrast to noble metal plasmonic structures, where absorption efficiencies approaching 100% have been experimentally realized.<sup>[76–78]</sup> This discrepancy is due to the low carrier density of graphene, which leads to a low oscillator strength, and correspondingly low absorption cross sections. In order to achieve high modulation efficiencies, the absorption cross section must be larger than the physical unit cell of the resonator array, which is difficult to achieve in atomically thin materials with low carrier densities.

To achieve strong light modulation in graphene plasmonic devices, intriguing strategies have been proposed. Stacking of graphene disks with insulating layers was utilized to enlarge the scattering cross sections, which resulted in improved light–matter interaction in graphene.<sup>[71]</sup> High doping levels with ionic gels<sup>[68,69]</sup> and double-layered graphene<sup>[79]</sup> were also exploited to increase oscillator strength in graphene nanoresonators. Furthermore, using a strategy borrowed from the radio antenna community, graphene nanoresonators with a back reflector have been theoretically expected to exhibit perfect absorption.<sup>[80]</sup> In this scheme illustrated in Figure 4a (a so-called Salisbury screen), the back reflector is designed to recycle photons escaping from the graphene nanoresonators, creating a Fabry–Perot resonance that enhances the electric field intensity in the graphene sheet. Subsequent experiments demonstrated that this strategy can enhance the absorption in graphene up to 25%, as shown in Figure 4a.<sup>[55]</sup>

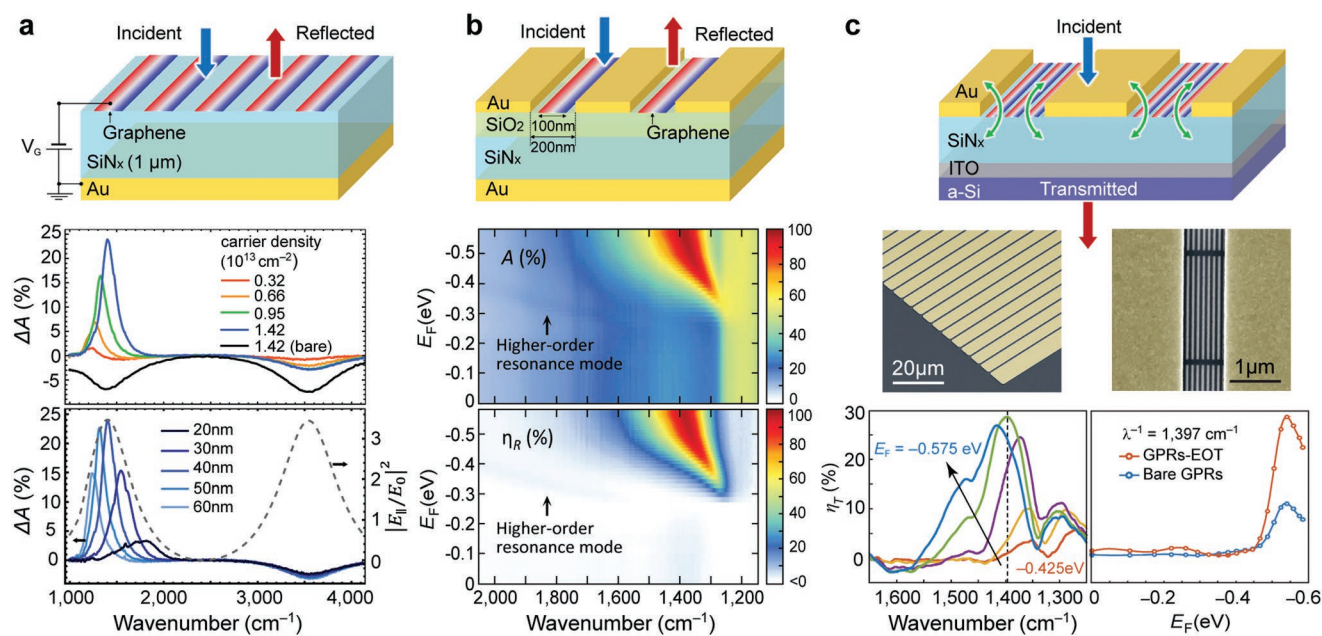


**Figure 4.** a) (Top) Schematic of graphene nanoresonators placed on a Salisbury screen. Measured mid-infrared light resonant absorption (middle) as varying the carrier densities of 40-nm-wide graphene nanoresonator and (bottom) as varying the graphene nanoresonator width with  $n = 1.42 \times 10^{13} \text{ cm}^{-2}$ . The dotted curve in the bottom spectra represents field enhancement from the Salisbury screen. Adapted with permission.<sup>[55]</sup> Copyright 2014, American Physical Society. b) (Top) Schematic of graphene nanoresonators incorporated with noble metal plasmonic antennas. (Middle) Measured gate-dependent absorption map exhibiting perfect absorption in graphene. (Bottom) Measured gate-dependent reflection modulation efficiency map ( $\eta_R = 1 - R/R_{\text{max}}$ ). Adapted with permission.<sup>[13]</sup> Copyright 2018, American Chemical Society. c) (Top) Schematic of graphene nanoresonators regulating the resonant transmission of noble metal plasmonic structures. (Middle) SEM images of a fabricated device. (Bottom) Measured gate-dependent transmission modulation efficiency ( $\eta_T = 1 - T/T_{\text{max}}$ ) exhibiting 2.7 times higher light modulation efficiency in the coupled structure compared with a bare graphene nanoresonator device. Adapted with permission.<sup>[53]</sup> Copyright 2016, Springer Nature.

Despite these efforts, strong light modulation using graphene nanoresonators has been elusive due to the inefficient coupling between the graphene plasmons and free space photons. This weak coupling is, in fact, related to the large confinement factors of graphene plasmons, which is—in principle—a desirable property, but also creates a large mismatch between the free space and graphene plasmon optical wavelengths.<sup>[56,81]</sup> In other words, scattering cross sections in graphene nanoresonators are limited by the inherent large momentum mismatch.

A second effect limiting coupling efficiency is the low mobility of the CVD graphene used in most optoelectronic devices, which degrades the plasmonic oscillator strength. In most graphene plasmonic light modulators, a CVD-grown graphene was preferably adopted because of its usability in fabrication and mass production. However, the use of CVD-grown graphene leads to degraded carrier mobility, a crucial factor determining the oscillator strength in graphene nanoresonators. Compared with high carrier mobilities achievable in exfoliated/encapsulated graphene, processed CVD-grown graphene layers inevitably exhibit much lower carrier mobilities because trapped impurities, wrinkles, and polymethyl methacrylate (PMMA) residues are unavoidable in transferring CVD graphene onto a substrate.<sup>[82,83]</sup> Moreover, patterning graphene itself diminishes graphene quality as it produces edge defects. In particular, narrower graphene nanoresonators suffer from more edge scattering, which results in low graphene carrier mobilities.<sup>[84]</sup> The carrier mobilities in patterned graphene

were estimated to be  $400\text{--}500 \text{ cm}^2 \text{ V}^{-1} \text{ s}^{-1}$  with  $\approx 0.5 \text{ eV}$  of graphene Fermi level.<sup>[13,53,55]</sup> In addition, scattering of graphene plasmons from the edges has been shown to increase the damping rate,<sup>[67]</sup> and plasmons along the edges were visualized in patterned graphene.<sup>[85]</sup> These defects induced in fabrication end up weakening the oscillator strength in graphene nanoresonators. At frequencies higher than  $0.2 \text{ eV}$  ( $\approx 1600 \text{ cm}^{-1}$ ), optical phonons in graphene are expected to provide an additional damping pathway for graphene plasmons.<sup>[37,67]</sup>

### 3.4. Multiscale Nanophotonic Design for Efficient Light Modulation

In order to ultimately overcome the weak interaction between graphene plasmons and free space light, strategies have emerged that use noble metal antenna structures that focus the light onto the graphene sheet, where multiscale nanophotonic design was utilized to significantly enhance the light–matter interactions in graphene. Figure 4b,c displays examples of two such devices.<sup>[13,53]</sup> Graphene nanoribbons were placed inside noble metal slits, and they were fabricated on an insulator/back reflector membrane. In this work, the incorporated noble metal antennas play two pivotal roles. First, the subwavelength-scale metal antennas help bridge the gap between free space photons and graphene plasmons at deep-subwavelength scale.<sup>[13]</sup> This configuration intermediates the large wavevector mismatch between them, so that radiative coupling to graphene

nanoresonators is improved. Second, nonresonant focusing effect by the noble metal antennas leads to a huge increase in oscillator strength of the graphene nanoresonators.<sup>[86,87]</sup> This improvement can also be understood by the enlargement of the scattering cross section of the graphene nanoresonators.

As a result of enhancing the light–matter “coupling” and the light–matter “interactions” in the graphene nanoresonators, it has been experimentally demonstrated that perfect absorption is no longer limited by low graphene carrier mobilities. Mid-infrared measurements demonstrated 97% of absorption in graphene nanoresonators incorporated with noble metal antennas, as shown in Figure 4b, while a bare graphene nanoresonator device exhibited only 52% of absorption.<sup>[13]</sup> Here, the extremely large absorption was realized by a resonant absorption in the graphene layer covering less than 10% of the surface area, and not in the incorporated noble metal plasmonic structures.

Multiscale nanophotonic design has also been adopted to efficiently regulate transmitted light using graphene nanostructures. Figure 4c illustrates how to modulate resonant transmission electronically with graphene plasmons.<sup>[53]</sup> The periodically arranged noble metal structures exhibit an extraordinary optical transmission (EOT) type effect.<sup>[88–90]</sup> The resonant transmission is achieved by coupled surface plasmons on the top and bottom surfaces of the metal grating with the metallic gap being their coupling channel. When the intergap graphene nanoresonators are tuned to exhibit resonant absorption at the EOT frequency, it blocks the coupling channel, resulting in the suppression of the resonant transmission. Similar to the schematic presented in Figure 4b, the incorporated noble metal structures enhance the oscillator strength of graphene nanoresonators, leading to a high modulation efficiency. In the experimental results presented in Figure 4c, the multiscale graphene nanoresonator device exhibited 2.7 times higher light modulation efficiency at mid-infrared compared with a bare graphene nanoresonator device.<sup>[53]</sup> Another efficient light modulation was also demonstrated at the THz range with a multiscale graphene nanoresonator structure.<sup>[91]</sup> In this structure, an anticrossing between the resonant absorptions in split-ring resonators and graphene nanoresonators was exploited to regulate the resonant transmission.

## 4. Molecular Sensing

Infrared spectroscopy is a powerful technique used in biochemistry and industry due to its label-free and nondestructive molecular identification capabilities. Most molecules have their own characteristic structural rotations and vibrations, and these roto-vibrational modes can be directly activated with mid-infrared light. By detecting the resonant spectral “fingerprints” in the mid-infrared, one can identify the molecular composition of target specimen. However, one major hurdle facing infrared spectroscopy is its relatively poor detection sensitivity originating from weak light–matter interactions between molecules and mid-infrared light. These weak interactions mainly arise from the fact that the molecules (usually below 10 nm) are much smaller than the wavelength of mid-infrared radiation.<sup>[92,93]</sup> In this section, we discuss how to improve the detection capability of infrared spectroscopy with polaritons in 2D materials.

### 4.1. Infrared Spectroscopy with Polaritons in vdW Materials

To overcome the weak light–molecule interactions in infrared spectroscopy, noble metal plasmonic structures have previously been exploited. These methods—known as surface enhanced infrared absorption (SEIRA)—leverage the plasmonic resonances in metallic structures to create hotspots of high light confinement, which leads to significant enhancement in local light–molecule interactions.<sup>[94,95]</sup> By tailoring the nanoantennas to exhibit plasmonic resonances at the vibration frequencies of target agents, strong absorption signals could be observed in the infrared, with enhancement in sensitivity of up to five orders of magnitude.<sup>[96]</sup> This method of using metal antennas to locally enhance optical fields is fully compatible with polaritonic vdW materials where the enhancement can be much higher due to the high confinement factors. Furthermore, in the case of dielectric vdW materials, the losses can be significantly reduced, leading to better resolved resonances. This has led to significant interests in using vdW materials for improved infrared spectroscopy.

Similar to graphene nanoresonators discussed in Section 3.2, the localized hyperbolic phonon polariton modes can be excited in patterned polar van der Waals crystals.<sup>[97–99]</sup> In patterned h-BN, hyperspectral resonances with Q-factors of 283 could be achieved due to the absence of electronic losses in h-BN.<sup>[99]</sup> In addition to the high Q-factor, a large confinement of  $\lambda_0/86$  was also realized,<sup>[99]</sup> which results in a strong near-field enhancement around the resonators.<sup>[98]</sup> Figure 5a illustrates how the h-BN nanoresonators were used for detecting the mid-infrared spectral features of C–H bond at  $1450\text{ cm}^{-1}$  in 4,4'-bis(N-carbazolyl)-1,1'-biphenyl (CBP).<sup>[33]</sup> Exfoliated h-BN flakes (40 nm thick) were transferred onto a  $\text{CaF}_2$  substrate, h-BN nanoribbons were patterned by the electron beam lithography followed by reactive ion etching. The ribbon width and the pitch were 158 nm and 400 nm, respectively. The CBP layers were deposited by thermal evaporation. Transmission measurement results presented in Figure 5a display strong light–molecule interactions when the hyperbolic phonon polariton resonance and the vibrational spectrum of the C–H bond in CBP are overlapped (blue curve, 20 nm-thick CBP).<sup>[33]</sup> Without the h-BN nanoresonators, the clear spectral feature disappears (lower brown curve, 20 nm-thick CBP), which originates from the inherent size discrepancy between the mid-infrared wavelength and the molecules. Due to the high Q-factor in the hyperbolic phonon polariton nanoresonators, their molecular detection performance is anticipated to significantly surpass the conventional SEIRA based on noble metal plasmonic structures.

### 4.2. Dynamic Infrared Spectroscopy

In order to enhance molecular detection performance, the SEIRA method requires matching the resonance frequency of incorporated resonators to the roto-vibrational frequencies of the target molecules. This asserts the importance of tunability of the plasmonic resonant frequency to cover a variety of molecular fingerprints appearing throughout a wide range of mid-infrared frequencies. However, it is not straightforward to integrate tunability into the conventional nanophotonic

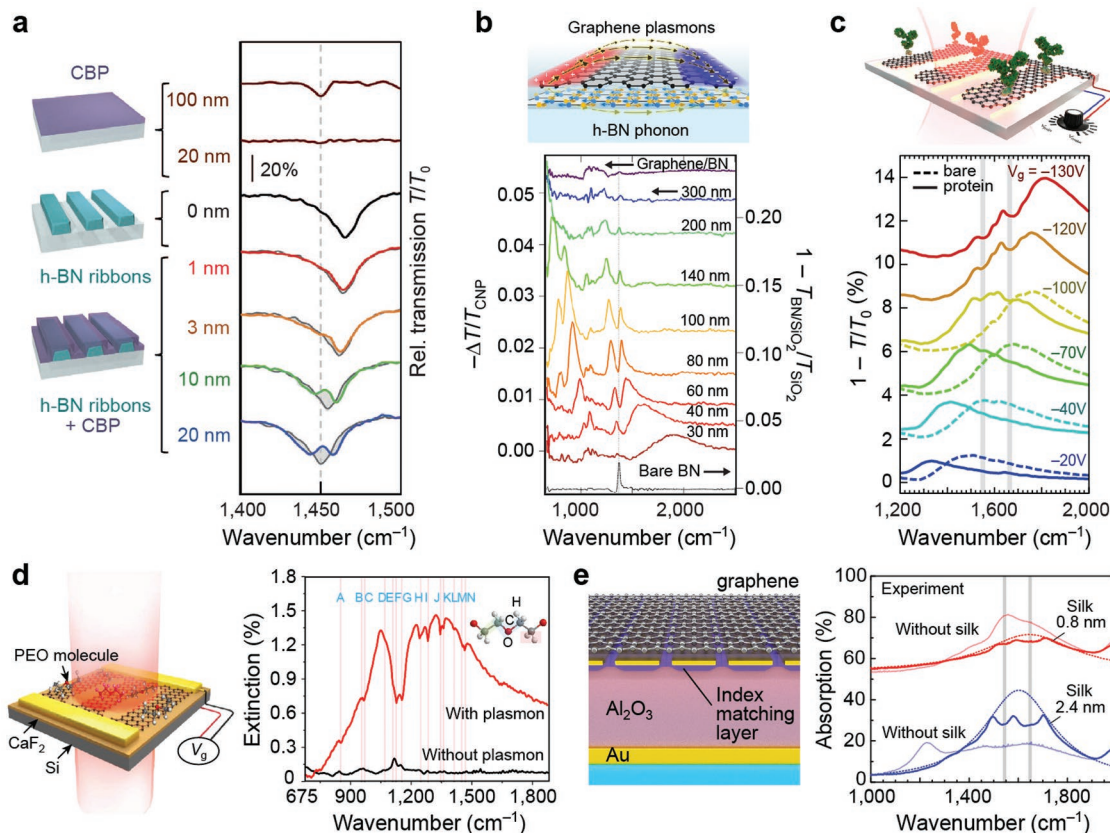


**Figure 5.** a) (Left) h-BN ribbon arrays with CBP. The ribbon width and the period are 158 nm and 400 nm, respectively. (Right) Measured transmission spectra with different CBP thicknesses. The gray dashed line at 1450  $\text{cm}^{-1}$  corresponds to the C–H vibrational frequency in CBP, and clear spectral features appear when the resonance of the h-BN ribbons match to that frequency. Adapted with permission.<sup>[33]</sup> Copyright 2018, Springer Nature. b) (Top) Illustration of hybridized SPPP modes in a graphene/monolayer h-BN nanoresonator. (Bottom) Measured transmission spectra as varying the nanoresonator width. Sharp dips at 1370  $\text{cm}^{-1}$  arise from the SPPs in the heterostructure. Adapted with permission.<sup>[100]</sup> Copyright 2014, American Chemical Society. c) (Top) Schematic of graphene nanoresonators detecting protein molecules. (Bottom) Measured extinction spectra as varying the doping level of the graphene nanoresonators. Gray vertical strips indicate amide I and II vibrational bands of the protein. Adapted with permission.<sup>[92]</sup> Copyright 2015, AAAS. d) (Left) Molecular detection with graphene nanoresonators on a  $\text{CaF}_2$  insulating layer. (Right) Measured extinction spectra covering a wide range of mid-infrared. Adapted with permission.<sup>[101]</sup> Copyright 2016, Springer Nature. e) (Left) Schematic of acoustic graphene plasmonic device. Target molecules are placed beneath the graphene sheet. (Right) Measured absorption spectra detecting thin silk layers. Gray vertical strips indicate amide I and II vibrational bands of the silk layer, and dashed lines are calculated from Lorentzian fitting. Adapted with permission.<sup>[108]</sup> Copyright 2019, Springer Nature.

structures as their plasmonic resonance frequencies are predetermined at the time of fabrication. In other words, their resonances are static, and can only interact with the molecular vibrations that fall within a fixed frequency window. In atomically thin vdW materials, however, the plasmon polaritons can be tuned by changing the sheet carrier density, which allows for the realization of devices that can be electrostatically controlled to sweep over a wide frequency range, and also leverage the strong field confinement in vdW materials to increase sensitivity.<sup>[93]</sup>

As discussed in Section 3.2, graphene plasmons exhibit electronically tunable electromagnetic behavior, which enables an active light modulation with graphene nanoresonators. In addition to the tunability, highly confined graphene plasmons yield strong near-field enhancement, indicating promising potentials for SEIRA. In particular, enhanced light–matter interactions with graphene nanoresonators were demonstrated for the identification of monolayer h-BN.<sup>[100]</sup> In this work,

graphene nanoresonators were fabricated on a monolayer h-BN sheet, as shown in Figure 5b. When the resonance in the graphene nanoresonators is tuned to the optical phonon in h-BN at 1370  $\text{cm}^{-1}$  (gray vertical line in Figure 5b), highly confined near-fields of the graphene plasmons boost up the interactions with the monolayer h-BN, producing hybrid surface-phonon-plasmon-polariton modes in the heterostructure.<sup>[100]</sup> The degree of interaction can be controlled by varying the size of the nanoresonators, or by electrostatically tuning them. As the plasmon and phonon resonances are moved relative to one another, they exhibit an anticrossing in frequency space that results from the strong interaction between them. As a result, a clear dip in transmission appears despite the h-BN sheet being only atomically thin, as shown in Figure 5b, indicating that graphene nanoresonators can be utilized for extremely sensitive molecular detection.

The tunable properties and the strong near-field enhancement in graphene nanoresonators have been experimentally

demonstrated to identify the mid-infrared molecular responses from a small amount of organic specimens to gas molecules.<sup>[92,101–104]</sup> Figure 5c illustrates the basic schematic of electronically tunable SEIRA with graphene nanoresonators detecting protein molecules.<sup>[92]</sup> The plasmonic resonance in the graphene nanoresonators is controlled by electrostatic gating, and target protein molecules are placed on the graphene. When the plasmonic resonance is tuned to the vibrational bands of the protein (gray vertical strips), the resonant coupling between them produces two spectral dips at the vibrational frequencies, as shown in Figure 5c, which indicates the presence of the protein molecules. These spectral dips are almost undetectable when they are off-resonance ( $V_g = -20$  or  $-40$  V), revealing the importance of tunability in SEIRA spectroscopy.

One major issue expected in SEIRA spectroscopy with graphene nanoresonators would be a limited coverable spectral range due to substrate. Most commonly used insulating layers, such as  $\text{SiO}_2$ ,  $\text{SiN}_x$ ,  $\text{Al}_2\text{O}_3$ , or  $\text{HfO}_2$ , have strong phononic absorption usually below  $1100\text{ cm}^{-1}$ , where the damping rate of the graphene plasmons becomes too high to yield a strong resonance. Although h-BN could be considered as an alternative insulating material, the in-plane and out-of-plane phonons lead to producing blind spectral regions at the vicinities of  $1360$  and  $760\text{ cm}^{-1}$ , respectively. To resolve this problem,  $\text{CaF}_2$  was used as an alternative insulating layer to gate graphene nanoresonators.<sup>[101]</sup> Compared to other insulating materials,  $\text{CaF}_2$  has almost zero phononic absorption up to  $650\text{ cm}^{-1}$ , making its optical properties suitable for SEIRA spectroscopy.<sup>[105]</sup> With the use of a  $\text{CaF}_2$  insulating layer, graphene nanoresonators were demonstrated to identify a molecule's vibrational fingerprints ranging from  $844$  to  $1466\text{ cm}^{-1}$ ,<sup>[101]</sup> as shown in Figure 5d, where the vibrational spectral features turn out to be obscure without the graphene plasmons.

### 4.3. Acoustic Plasmons with Atomic-Scale Vertical Field Confinement

2D polaritons are vertically confined with the characteristic length of  $\lambda_p/\pi$ . For example, if graphene plasmons exhibit a confinement factor of  $n_{\text{eff}} \approx 100$  at free space wavelength  $\lambda_0 = 10\text{ }\mu\text{m}$ , then  $\lambda_p/\pi \approx 30\text{ nm}$ , and its electric field reaches up to  $\approx 30\text{ nm}$  away from the graphene surface. Recently, it has been discovered that a graphene–insulator–noble metal heterostructure can overcome this vertical confinement limit and squeeze the field of plasmon polaritons in the length scale of one atomic layer, since the noble metal prevents the field penetration by inducing the image charges on its surface.<sup>[14]</sup> This new plasmonic mode is called “acoustic” graphene plasmons (named so for their linear dispersion and symmetric field profile, resembling the acoustic phonon modes in graphene) and exhibits higher lateral confinement ( $n_{\text{eff}}$  up to  $\approx 170$ ) compared to regular graphene plasmons.<sup>[14,20,106]</sup> Systems with such extreme plasmon confinement go into the nonlocal regime,<sup>[106]</sup> while the momentum of acoustic graphene plasmons approaches the fundamental limit imposed by the Landau damping. Such acoustic plasmons are also theoretically expected to exist in BP, exhibiting anisotropic dispersion in the mid- and far-IR regimes.<sup>[107]</sup>

The extremely high near-field confinement of acoustic graphene plasmons was recently used to realize ultrasensitive infrared spectroscopy, as shown in Figure 5e.<sup>[108]</sup> In this device, acoustic graphene plasmons on metal strips were launched by intergap graphene plasmons excited from metal edges. A thin silk protein layer was placed beneath the graphene sheet, and a back reflector was incorporated to further enhance light–matter interactions, which resulted in large absorption. As shown in Figure 5e, two spectral dips emerged at the vibrational frequencies of the target silk protein. In particular, even an angstrom-thick protein was detectable due to the extreme level of light–matter interactions.<sup>[108]</sup>

## 5. Thermal Radiation Engineering

Any object at temperatures from  $300$  to  $1000\text{ K}$  emits thermal radiation at mid-infrared frequencies. Until recently, the thermal emission characteristics of an object was considered to be fixed and not actively controllable, and that the intensity of thermal emission was upper bounded by the Planck's thermal radiation law. Recent advances in nanophotonics, however, have challenged this conventional conception.<sup>[109]</sup> By employing exotic polaritonic properties of van der Waals crystals, the characteristics of thermal emission can be substantially engineered to realize dynamic thermal emission modulation<sup>[15]</sup> and super-Planckian radiative heat transfer.<sup>[16,110–112]</sup>

### 5.1. Dynamic Modulation of Thermal Emission

Dynamic modulation of thermal radiation is desirable for many applications based on tunable mid-infrared sources including compact IR spectroscopy, chemical analysis, and environmental monitoring.<sup>[15,113]</sup> The most straightforward method to modulate the thermal emission intensity is to adjust the temperature of the emitter. However, temperature modulation is often inefficient and slow since heating and cooling of macroscopic objects having large heat capacity requires a large amount of energy and takes a long time. An alternative way of modulating thermal emission intensity is to control the emissivity of the object. Kirchhoff's law of thermal radiation states that the angular spectral emissivity  $e(\omega, \hat{n}, \hat{p})$  is equal to the angular spectral absorptivity  $\alpha(\omega, \hat{n}, \hat{p}^*)$  for reciprocal thermal emitters, where  $\hat{n}$  and  $\hat{p}$  specify the direction and the polarization, respectively. Consequently, optical devices that can modulate the absorption of incident light can also modulate its own thermal emission dynamically. The direction, polarization, and the spectral line shape of thermal emission can also be controlled by engineering the absorption characteristics of the emitter.<sup>[109]</sup>

Electrically tunable plasmon polariton resonances in graphene nanostructures, which were introduced in Section 3, can also be utilized in dynamic thermal emission modulation. Brar et al. demonstrated that the thermal radiation of graphene plasmonic resonators on  $\text{SiN}_x/\text{Au}$  substrate can be dynamically tuned by varying the graphene carrier density via electrostatic gating,<sup>[15]</sup> as schematically shown in Figure 6a. The changes in emissivity spectra have a peak at the plasmon resonance frequency and the intensity of the peak substantially increases and

its spectral position blueshifts from around 1300 to 1400  $\text{cm}^{-1}$  as the carrier density varies from 0.5 to  $1.2 \times 10^{12} \text{ cm}^{-2}$  as shown in Figure 6b. The emissivity spectrum is also strongly dependent on the polarization, reconfirming that the peak originates from the graphene plasmon resonance (Figure 6c). As predicted by Kirchhoff's law of thermal radiation, the emissivity and the absorptivity spectra of the device at the same carrier density match well. The maximum thermal power modulation is observed to be  $50 \text{ pW cm}^{-1}$  at  $250 \text{ }^\circ\text{C}$  which compares favorably with commercial mid-infrared LEDs. The switching speed of the electronic thermal emission modulation is limited by the RC time constant rather than the heat capacity or thermal time constant of the device.<sup>[15]</sup>

## 5.2. Super-Planckian Radiative Heat Transfer

Planck's law for black bodies sets an upper limit for the radiative heat transfer between macroscopic objects in the far-field. However, since the Planck's law is based on ray optics, it fails to describe the radiative heat transfer in two distinctive regimes where either (1) the separation between the objects or (2) the dimensions of the objects are smaller than the thermal wavelength (about  $10 \text{ }\mu\text{m}$  at room temperature).<sup>[114]</sup> The extremely confined and anisotropic nature of the polaritons in vdW crystals, along with their atomic thinness, provide an ideal platform to access both regimes and thus realize the super-Planckian radiative heat transfer.

When two objects are put in close vicinity (separation  $<$  thermal wavelength), the evanescent waves of the two objects can couple together and provide extra channels for the radiative heat transfer. The rate of this near-field radiative heat transfer (NFRHT) is thus strongly dependent on the near-field density of photonic states in the system, which can be enhanced and tuned by the highly confined ( $n_{\text{eff}} \approx 100$ ) polaritonic modes sustained by vdW crystals.<sup>[115]</sup> It was theoretically predicted<sup>[114,116]</sup> and experimentally demonstrated<sup>[117]</sup> that plasmons in graphene mediate and boost the NFRHT between polar dielectrics. In their recent experiments, Yang et al.<sup>[16]</sup> observed super-Planckian NFRHT between two macroscopic graphene sheets separated by  $430 \text{ nm}$  vacuum gap (Figure 6d), which exceeds the blackbody limit by 4.5 times for a wide range of temperature differences, as shown in Figure 6e.

Anisotropic polaritons in vdW materials not only make the NFRHT dependent on the crystal direction of the vdW materials<sup>[118]</sup> but also provide another path to further intensifying the NFRHT when they become hyperbolic.<sup>[110,112]</sup> Hyperbolic polaritons can possess arbitrarily large wavevectors. The near-field density of photonic states dramatically increases due to the contribution of these high- $k$  modes in a broad frequency regime.<sup>[119]</sup> Recently, Ge et al.<sup>[110]</sup> and Zhang et al.<sup>[118]</sup> theoretically investigated the NFRHT between the two suspended sheets of BP, and reported that the radiative heat flux can exceed the Planck's limit by  $10^2$  to  $10^4$  times for separation distance between 100 and 10 nm (Figure 6f,g). Liu and Zhang proposed periodic graphene ribbon arrays to induce hyperbolic modes and predicted a giant enhancement of the NFRHT by more than one order of magnitude.<sup>[112]</sup> Additionally, due to the low electronic heat capacity and large polaritonic field concentration,

the NFRHT between nanostructured vdW crystals can be ultrafast and the radiative cooling between two graphene nanodisks is predicted to occur within a femtosecond timescale.<sup>[120]</sup>

Planck's law is also expected to fail to describe the radiative heat transfer between sub-thermal-wavelength objects. Very recently, it was predicted<sup>[121]</sup> and demonstrated<sup>[122]</sup> that even the far-field radiative heat transfer (FFRHT) can overcome the Planckian limit by orders of magnitudes if some, not necessarily all, of the dimensions of the objects become much smaller than the thermal wavelength. Fernandez-Hurtado et al. theoretically investigated the ultimate limit of the far-field violation of Planck's law by analyzing the FFRHT between 2D materials (graphene and monolayer BP) in a coplanar configuration as shown in the insets of Figure 6h, and predicted more than seven orders of magnitude stronger FFRHT compared to the Planck's blackbody limit (Figure 6h).<sup>[111]</sup>

## 6. Polaritonic Dispersion Engineering in van der Waals Crystals

The electromagnetic field of the (quasi)particles in 2D materials stretches beyond the atomically thin layer, which makes them extremely sensitive to their proximity to substrates or other 2D crystals.<sup>[123]</sup> Furthermore, since the unique properties of 2D crystals stem from the periodicity of their atomic structure, free carriers and polariton species populating such materials are highly susceptible to the perturbation of the crystalline atomic structure. Therefore, properties of polaritons in 2D materials can be engineered at the quantum level via: (1) vertical stacking of vdW crystals, which leads to a hybridization of polariton species<sup>[100,124,125]</sup> or control over the level of their anisotropy;<sup>[126]</sup> (2) imposing a superlattice periodicity on 2D materials, which causes significant alteration on the polariton characteristics in nontrivial manner.<sup>[17,127–131]</sup>

### 6.1. Polaritons in van der Waals Heterostructures

Besides the straightforward engineering of interface properties,<sup>[132–135]</sup> stacks of vdW materials can support hybridized polaritonic modes. For example, in an h-BN-graphene heterostructure, graphene plasmons and h-BN phonons hybridize into infrared surface plasmon–phonon polaritons.<sup>[100,124,125]</sup> This new polaritonic species has been observed using both single- and multilayer h-BN, stacked with a single graphene layer. In the former case, the far-field measurements revealed the splitting of graphene plasmon dispersion into two optical modes with anticrossing near the frequency of the planar h-BN phonons.<sup>[100]</sup> The unique behavior is explained within the limits of classical electromagnetic coupling between the plasmonic near-field and the phonon modes of the h-BN lattice. In the case of multilayer h-BN substrate, the hybridization with hyperbolic phonons results in hyperbolic plasmon–phonon polaritons.<sup>[124]</sup> These hybridized infrared polaritons have been observed with the near-field technique, and demonstrated to have approximately twice larger propagation length compared to graphene plasmons due to lower sensitivity to ohmic losses in graphene.<sup>[124]</sup>

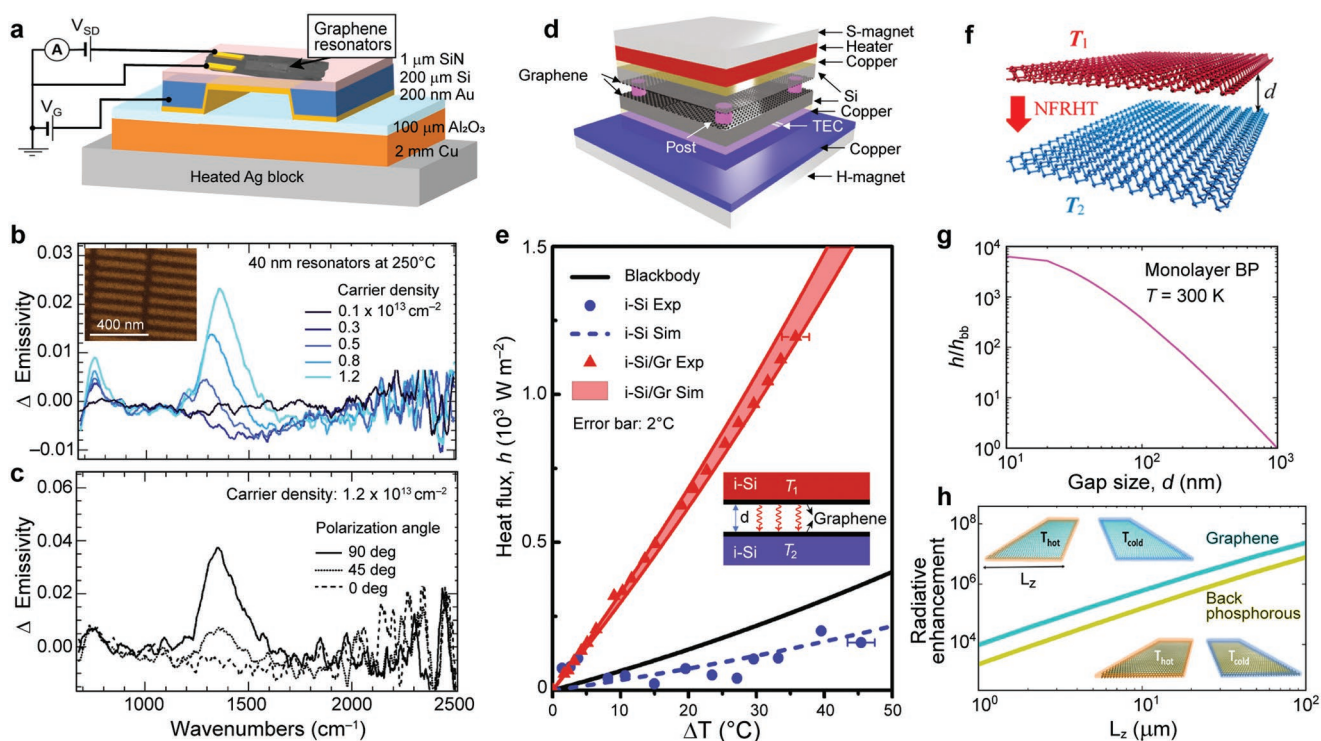


**Figure 6.** a) Graphene resonators array placed on the temperature-controlled stage with electrostatic gating for emissivity measurements. b) Carrier density dependence of change in emissivity with respect to the CNP for 40 nm graphene nanoresonators (inset) at 250 °C. c) Polarization dependence of the emissivity change for 40 nm graphene nanoresonators at 250 °C, for a carrier density of  $1.2 \times 10^{13} \text{ cm}^{-2}$ . (a–c) Adapted with permission.<sup>[15]</sup> Copyright 2015, Springer Nature. d) A schematic of the NFRHT measurement setup with vacuum between the emitter and receiver graphene layers. e) The measured heat flux density (symbols) and the analytical prediction (shaded region and dashed line) at different emitter temperature variation between i-Si substrates with or without graphene, as indicated; in the simulation, the gap between the layers is considered as  $d = 430 \pm 25 \text{ nm}$  and graphene's Fermi level  $E_F = 0.27 \pm 0.03 \text{ eV}$  (inset). (d,e) Adapted with permission.<sup>[16]</sup> Copyright 2018, Springer Nature. f) Schematic of the NFRHT between two monolayer BP sheets separated by the gap with size  $d$ . g) Ratio between the NFRHT and black body heat transfer rates as a function of  $d$ ; electron density  $n = 5 \times 10^{12} \text{ cm}^{-2}$ . (f,g) Adapted with permission.<sup>[118]</sup> Copyright 2018, American Chemical Society. h) FFRHT enhancement dominated by the TE-polarized guiding modes in the nanoribbons of graphene and BP. Adapted with permission.<sup>[111]</sup> Copyright 2018, American Chemical Society.

Interestingly, it is also possible to induce anisotropy to the dispersion of polaritons in an isotropic 2D material by stacking it with an anisotropic one. For example, in a very recent experimental study, Chaudhary et al. demonstrated h-BN phonon polaritons exhibiting an in-plane anisotropy induced by the BP substrate.<sup>[126]</sup> The study demonstrates the anisotropy of 1.25 for the phonons in 40 nm-thick layer of h-BN at  $1405\text{--}1440 \text{ cm}^{-2}$ , caused by the strong in-plane anisotropy of BP, as discussed in Section 2.2.

## 6.2. Plasmonics in Graphene Superlattices

It has been demonstrated that  $N$  layers of graphene exhibit  $N$  times the higher optical conductivity, since the electronic systems of the layers typically stay decoupled.<sup>[136]</sup> However, when the layers of graphene become electronically coupled, the plasmonic dispersion of system of the two graphene layers (bilayer graphene with Bernal stacking) significantly deviates from that of a single layer, characterized by a higher plasmon momentum, which has been associated with the interlayer tunneling.<sup>[137]</sup> The system of bilayer graphene has one more degree of freedom: the twist angle  $\theta$  between the layers, leading to the formation of a moiré superlattice of carbon atoms, as

shown in **Figure 7a**. When the twist angle is large ( $\theta \gtrsim 3^\circ$ ), the period of the moiré superlattice is small enough to consider the twisted bilayer graphene (TBG) as a uniform material, having continuous band structure which depends on the twist angle<sup>[138–140]</sup> (Figure 7b) and can be electrostatically tuned.<sup>[138]</sup> Accordingly, the plasmonic dispersion in TBG also depends on  $\theta$ . Hu et al.<sup>[141]</sup> probed the infrared graphene plasmons in single-layer graphene (SLG) and TBG with different twist angles using the s-SNOM at excitation wavelength  $\lambda_0 \approx 11 \mu\text{m}$  (Figure 7c). According to the measurements, the plasmon dispersion in TBG is close to that of SLG at smaller angles, while shifting to larger plasmonic wavelengths (and hence, lower damping) as the angle increases.<sup>[141]</sup> From the analytical model for conductivity in both cases, the estimated SLG plasmon wavelength was  $\lambda_p^{\text{SLG}} \approx 279 \text{ nm}$ , while the plasmon wavelength in TBG was  $\lambda_p^{\text{TBG}} \approx 393, 387, 340, \text{ and } 278 \text{ nm}$  for  $\theta \approx 27^\circ, 12^\circ, 5^\circ, \text{ and } 3^\circ$ , respectively. Authors noted that the measured  $\lambda_p^{\text{TBG}}$  agrees well with the theoretical model for TBG in the Dirac regime<sup>[139]</sup> only at large twist angles  $\theta \gtrsim 3^\circ$ . However, when the twist angle is small, the TBG system goes into a completely different regime, for example, exhibiting unconventional physical properties at the “magic angle” of  $\theta \approx 1.1^\circ$ ,<sup>[142]</sup> which has caused much excitement across the broader physics community.

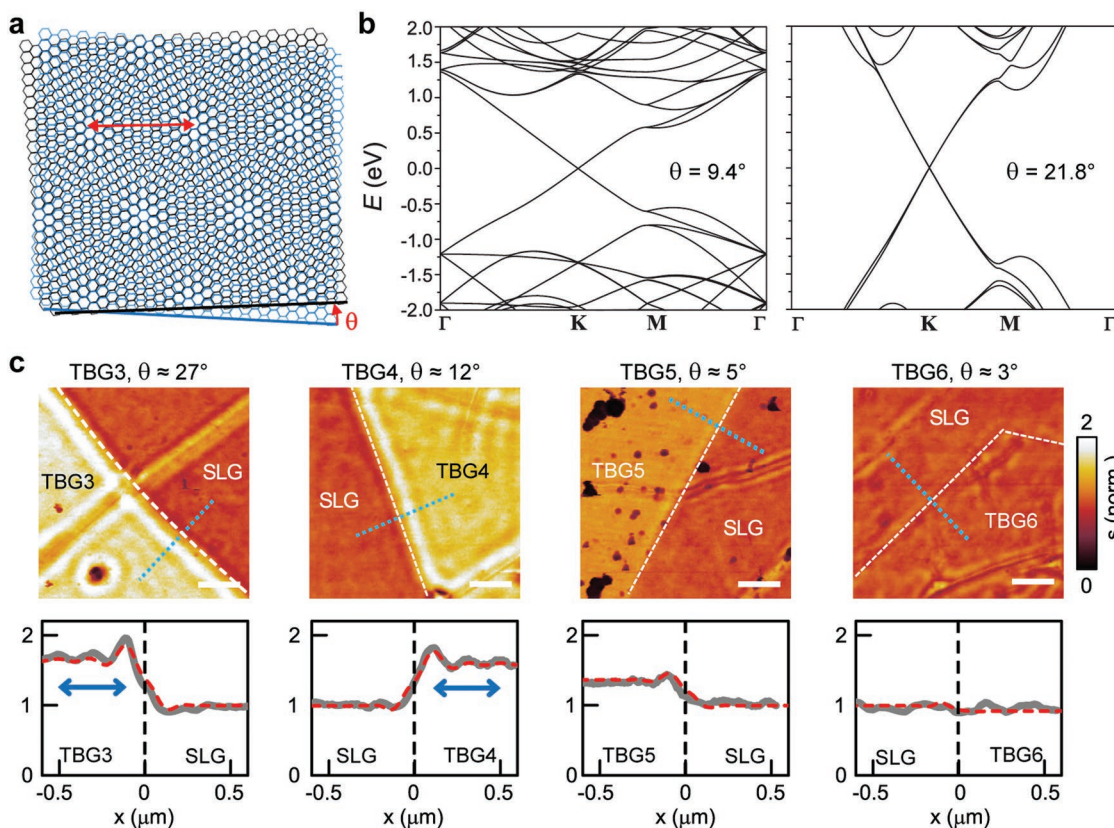


**Figure 7.** a) Schematics of the moiré superlattice in TBG with twist angle  $\theta$ , with period indicated by the red arrow. Adapted with permission.<sup>[141]</sup> Copyright 2017, American Physical Society. b) Calculated electronic band structure of TBG for the indicated  $\theta$ . Adapted with permission.<sup>[140]</sup> Copyright 2013, American Physical Society. c) (Top row) Map of the near-field amplitude  $s$  showing the boundary between SLG and TBG with different twist angle; plasmonic fringes clearly visible. (Bottom row) Model (red dashed) and measured (gray solid) near-field amplitude profile across the interfaces (indicated by the dashed blue line); blue arrow marks the plasmonic wavelength in TBG, twice larger than the fringe period. Adapted with permission.<sup>[141]</sup> Copyright 2017, American Physical Society.

For even smaller twist angles  $\lesssim 1^\circ$ , the period of the moiré superlattice ( $\approx 10\text{--}100$  nm) becomes significantly larger than that of the graphene atomic lattice. This allows atoms in the two adjacent graphene sheets to reconstruct their lattices into energetically favorable AB and BA Bernal stacking, thus forming commensurate domains of different stacking order separated by domain walls of topological nature<sup>[17,131,143–145]</sup> as shown in **Figure 8a**. These domain walls support topological chiral states, causing the local conductivity to increase due to the optical transitions between the chiral states and band continua<sup>[17,144]</sup> (**Figure 8b**). Jiang et al.<sup>[144]</sup> experimentally observed the electrically tunable reflection of propagating infrared plasmons at the topological boundaries with the near-field imaging technique (**Figure 8c**). And more recently, Sunku et al.<sup>[17]</sup> used the near-field imaging to demonstrate the interference of plasmon polaritons in the network of the topological domain walls. In fact, it has been suggested that the superlattice of the topological domain boundaries can be potentially used as a tunable photonic crystal for infrared graphene plasmons: theoretical calculations predict an opening of a bandgap in the plasmonic dispersion due to the presence of the superlattice formed by the domain walls with large enough plasmon scattering strength<sup>[17]</sup> (**Figure 8d**). The electrostatic and micromechanical (via twist angle) tunabilities of such superlattices are

promising mechanisms to control highly confined graphene plasmons and other polaritons in layered van der Waals materials at the quantum level, without the demanding top-down nanofabrication.

Another platform that allows formation of periodic moiré superlattices is the heterostructure of graphene and h-BN, since both materials have similar lattice constants as well as strong interlayer coupling between carbon atoms in graphene and boron and nitrogen atoms in h-BN.<sup>[146,147]</sup> With careful lattice matching, it is possible to create a moiré superlattice domain of moderate size (of sub-micrometer scale and up to  $\approx 10$  nm period) where electronic bands of graphene are significantly perturbed, acquiring a new set of superlattice-induced Dirac minibands, leading to a nontrivial plasmonic dispersion.<sup>[129,130,147]</sup> Once again, the near-field imaging technique was used for the experimental investigation of this phenomenon<sup>[129]</sup> (**Figure 8e**). Although the exact physical model of graphene plasmons in h-BN-induced superlattice is still under development, the most recent theoretical investigation suggests that the graphene/h-BN moiré superlattice leads to a strong asymmetry in the electronic dispersion of graphene between the hole and electron doping regimes,<sup>[130]</sup> a trait that is drastically different from that of a single-layer graphene.<sup>[35]</sup>

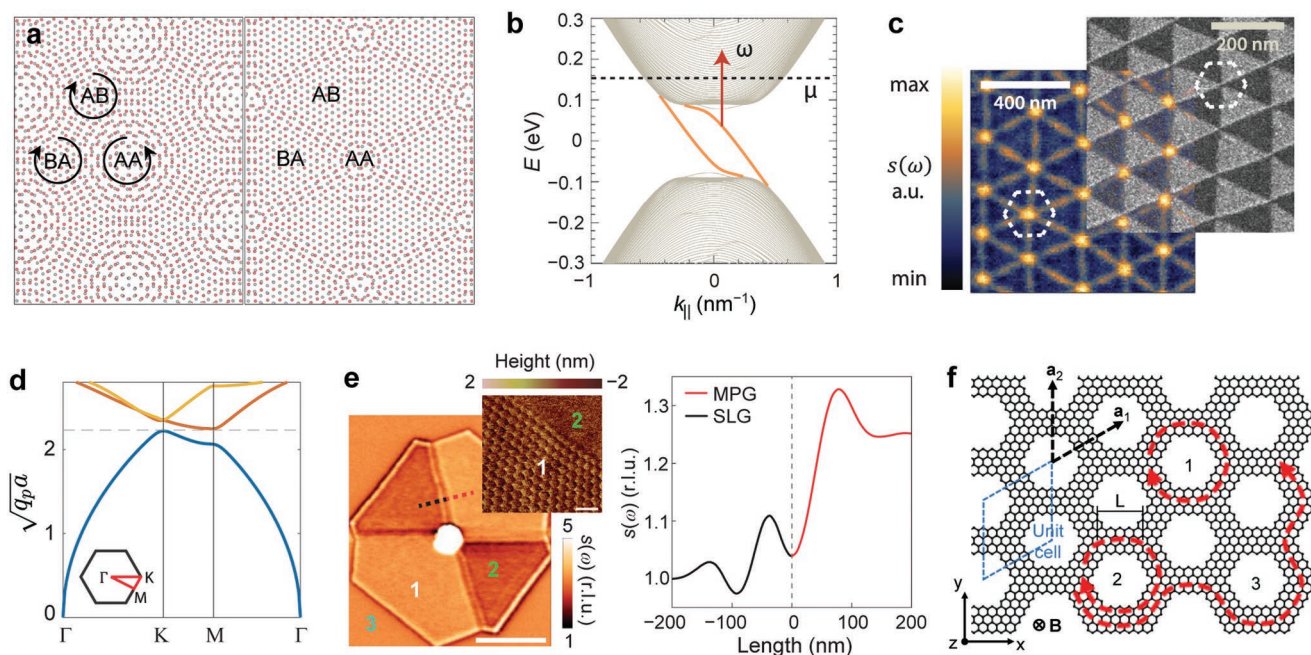


**Figure 8.** a) Schematics of the TBG with small twist angle before (left) and after (right) lattice reconstruction. Adapted with permission.<sup>[143]</sup> Copyright 2019, Springer Nature. b) Electronic band structure of the topological domain wall ( $K$  valley) with chiral 1D states (orange), red arrow indicates optical transitions responsible for the increased local conductivity. c) Near-field image of TBG (scattered field amplitude  $s$ ) with clearly visible topological boundaries, overlapped with TEM image of the TBG after reconstruction, showing domains of AB and BA stacking. d) Calculated plasmonic dispersion in the superlattice of topological boundaries with large plasmon scattering strength. (b–d) Adapted with permission.<sup>[17]</sup> Copyright 2018, AAAS. e) (Left) Near-field image of graphene on h-BN (scattered field amplitude  $s$ ) with domains of moiré-patterned graphene (“1”; MPG), graphene without moiré superlattice (“2”; SLG), and bare h-BN (“3”), scale bar is 1  $\mu\text{m}$ ; inset: surface mapping (AFM in contact mode) of the boundary between the domains of MPG (“1”) and SLG (“2”), scale bar in 40 nm. (Right) Scattered near-field amplitude across the MPG-SLG boundary, showing plasmonic fringes of different period. Adapted with permission.<sup>[129]</sup> Copyright 2015, Springer Nature. f) Topologically protected plasmons in graphene superlattice with broken  $T$  symmetry. Adapted with permission.<sup>[149]</sup> Copyright 2017, Springer Nature.

Finally, graphene is predicted to become a platform for the realization of topologically protected infrared plasmons in a periodically patterned single layer<sup>[148,149]</sup> (Figure 8f). In general, topological optical states require the time-reversal symmetry ( $T$ ) breaking of the system’s optical response.<sup>[150]</sup> Due to its low dimensionality, graphene is predicted to provide  $T$ -breaking for the edge-bound plasmonic modes under relatively low magnetic fields of  $\approx 1$  tesla.<sup>[148]</sup> However, topological plasmons are yet to be experimentally demonstrated.

## 7. Outlook

The unique electronic properties of van der Waals materials combined with their intrinsic thinness and smoothness allow them to exhibit distinctive optical properties that are of both fundamental and technological interest. Thus far, those properties—which include high mode confinement, index tunability, and optical anisotropy—have been observed and leveraged in only a small number of potential material systems, including graphene, h-BN, black phosphorus, and  $\alpha\text{-MoO}_3$ . However, there is a large number of alternative van der Waals materials that can exhibit these properties including transition metal dichalcogenides, borophene, and more exotic materials such as  $\text{Bi}_2\text{Se}_3$ —a topological insulator that could support low loss plasmonic modes.<sup>[151]</sup> Many of these materials have already

been isolated for electrical studies, but they are difficult to integrate into optical devices due to either their air sensitivity, low sample quality, or an inability to fabricate large-scale samples. Fortunately, many of the characterization and device integration methods described in this progress report can be straightforwardly applied to new material systems. In particular, scattering SNOM has emerged as a powerful tool that can extract the localized polaritonic properties of small exfoliated samples that could not be probed in a conventional optical microscope.  $s$ -SNOM has recently been extended for use in low-temperature and high-vacuum environments,<sup>[41]</sup> and it can also be used to image samples that are encapsulated in h-BN, which can protect materials from environment. Furthermore, the device geometries that have been designed to optimize electrostatic gating and interactions with free space light can be broadly repurposed for many vdW materials.

Among the fundamental mid-infrared optical properties that will continue to attract interest in vdW material systems is their large confinement factors, high anisotropy, and the ability to create a tunable optical response over a large wavelength range. Materials with strong in-plane anisotropy, for example, could be used for hyperlensing, strong light–matter interactions, and directional light propagation. In addition to exploring materials with natural structural anisotropy, the application of strain or layering of two anisotropic materials could be used to alter the anisotropic optical properties in a controllable

manner. Furthermore, materials that display tunable, anisotropic plasmon polaritons, such as BP, could be developed into polarization switchers, or electrically tunable dichroic filters. For BP, some recent experiments to that end have been performed by exploiting BP's bulk electronic anisotropy,<sup>[152]</sup> but the use of surface plasmons requires better control of the BP surface. One alternative method of realizing such behavior is to couple the tunable surface plasmons of graphene with the anisotropic phonon polaritons of an underlying material, such as  $\alpha$ -MoO<sub>3</sub>. In that scheme, tunable hybrid modes could be realized that display anisotropy. Meanwhile, in order to increase the confinement factors in vdW optical materials, it is necessary to explore materials with lower polaritonic group velocities. To that end, systems with larger carrier effective masses could be explored, or higher purity samples could be developed with losses sufficiently small to allow polaritons to propagate even as the dispersion bands flatten. For plasmonic materials, decreasing the loss in the material could allow for plasmon polaritons to propagate even at very low carrier densities, where the confinement factors are increased.<sup>[37]</sup>

Integrating vdW materials with nanophotonic structures—including metasurfaces, photonic crystals (PC), waveguides, and plasmonic antennas—will continue to be explored as a means of making novel optical properties observable macroscopically and useful for device integration. In general, these strategies work by either increasing the optical path length through the vdW system, or by focusing the free space light into the small volume of the vdW crystal so that the interaction is increased. For optical sensing, this strategy could be useful in improving the overall signal-to-noise ratio in devices by, for example, simultaneously coupling the highly confined vdW modes to a molecule of interest as well as a photonic structure that interact with the far-field. Nanophotonic structures can also be explored as a way of creating a more narrowband response in polaritonic vdW materials, which can be useful for sensing, as well as for thermal emission devices. For example, experiments with graphene coupled to photonic crystals have shown that the narrow reflection peak of a PC cavity can be turned on/off by controlling the interband transitions in graphene,<sup>[153]</sup> and more recently it has been shown that the thermal emission from a graphene sheet can also be coupled to a PC cavity.<sup>[154]</sup> Improving the tuning range of vdW polaritons with nanophotonic structures, meanwhile, could be useful for the creation of dynamic phase shifter devices that can be used for spatial light modulators or holographic displays.<sup>[63,155]</sup>

Emerging many-body phenomena in vdW materials are extremely interesting from a polaritonic perspective, since the surface polaritons are intimately linked to the electronic and phononic structure of the material. Exploring how the optical response changes in twisted vdW systems, for example, could provide insight on the rich interactions in the material. As researchers continue to create material systems with novel physics, and rich phase transitions, it is likely that new polaritonic properties will become observable. As discussed before, twisted bilayer graphene is one exciting candidate material to observe such effects, but twisted transition metal dichalcogenide (TMD) layers can also show novel effects such as interlayer excitonic states that are confined within a tunable moire potential and emergent topological states.<sup>[156,157]</sup> Moreover, high-quality

graphene and bilayer graphene have recently been shown to display hydrodynamic properties and liquid nitrogen temperatures, which could affect plasmonic behavior.<sup>[158]</sup> Finally, several high  $T_c$  superconductors are also vdW materials,<sup>[159]</sup> and the polaritonic response in those systems could vary dramatically as they are brought to a single layer.

In summary, we anticipate that the development of mid-infrared polaritonics in vdW materials will not only give us deeper understanding of fundamental electronic and phononic interactions in solid-state systems but also lead to breakthroughs in practical applications including biosensing, environmental monitoring, modulation of mid-infrared light with unprecedented spatiotemporal resolutions, heat management beyond the Planck's limit, and thermal energy applications.

## Acknowledgements

S.K. and S.G.M. contributed equally to this work. This work was supported by the Samsung Research Funding Center of Samsung Electronics (SRFC-IT1702-14), by the National Research Foundation of Korea (NRF) grants funded by the Ministry of Science and ICT (2017R1E1A1A01074323 and 2019R1C1C1011131), and by the Gordon and Betty Moore Foundation through a Moore Inventors Fellowship.

## Conflict of Interest

The authors declare no conflict of interest.

## Keywords

active light modulation, light–matter interactions, mid-infrared regime, polaritons, van der Waals materials

Received: July 16, 2019

Revised: September 4, 2019

Published online: November 20, 2019

- [1] S. Subramanian, H. Y. Wu, T. Constant, J. Xavier, F. Vollmer, *Adv. Mater.* **2018**, *30*, 1801246.
- [2] A. B. Taylor, P. Zijlstra, *ACS Sens.* **2017**, *2*, 1103.
- [3] D. G. Baranov, Y. Xiao, I. A. Nechepurenko, A. Krasnok, A. Alu, M. A. Kats, *Nat. Mater.* **2019**, *18*, 920.
- [4] T. Low, A. Chaves, J. D. Caldwell, A. Kumar, N. X. Fang, P. Avouris, T. F. Heinz, F. Guinea, L. Martin-Moreno, F. Koppens, *Nat. Mater.* **2017**, *16*, 182.
- [5] D. N. Basov, M. M. Fogler, F. J. G. de Abajo, *Science* **2016**, *354*, aag1992.
- [6] D. Wintz, K. Chaudhary, K. Wang, L. A. Jauregui, A. Ambrosio, M. Tamagnone, A. Y. Zhu, R. C. Devlin, J. D. Crossno, K. Pistunova, K. Watanabe, T. Taniguchi, P. Kim, F. Capasso, *ACS Photonics* **2018**, *5*, 1196.
- [7] G. P. Neupane, K. Zhou, S. S. Chen, T. Yildirim, P. X. Zhang, Y. R. Lu, *Small* **2019**, *15*, 1804733.
- [8] Y. C. Fan, N. H. Shen, F. L. Zhang, Q. Zhao, H. J. Wu, Q. H. Fu, Z. Y. Wei, H. Q. Li, C. M. Soukoulis, *Adv. Opt. Mater.* **2019**, *7*, 1800537.
- [9] Q. S. Guo, C. Li, B. C. Deng, S. F. Yuan, F. Guinea, F. N. Xia, *ACS Photonics* **2017**, *4*, 2989.

- [10] Z. B. Zheng, J. N. Chen, Y. Wang, X. M. Wang, X. B. Chen, P. Y. Liu, J. B. Xu, W. G. Xie, H. J. Chen, S. Z. Deng, N. S. Xu, *Adv. Mater.* **2018**, *30*, 1705318.
- [11] W. L. Ma, P. Alonso-Gonzalez, S. J. Li, A. Y. Nikitin, J. Yuan, J. Martin-Sanchez, J. Taboada-Gutierrez, I. Amenabar, P. N. Li, S. Velez, C. Tollan, Z. G. Dai, Y. P. Zhang, S. Sriram, K. Kalantar-Zadeh, S. T. Lee, R. Hillenbrand, Q. L. Bao, *Nature* **2018**, *562*, 557.
- [12] Z. B. Zheng, N. S. Xu, S. L. Oscurato, M. Tamagnone, F. S. Sun, Y. Z. Jiang, Y. L. Ke, J. N. Chen, W. C. Huang, W. L. Wilson, A. Ambrosio, S. Z. Deng, H. J. Chen, *Sci. Adv.* **2019**, *5*, eaav8690.
- [13] S. Kim, M. S. Jang, V. W. Brar, K. W. Mauser, L. Kim, H. A. Atwater, *Nano Lett.* **2018**, *18*, 971.
- [14] D. A. Iranzo, S. Nanot, E. J. C. Dias, I. Epstein, C. Peng, D. K. Efetov, M. B. Lundeberg, R. Parret, J. Osmond, J. Y. Hong, J. Kong, D. R. Englund, N. M. R. Peres, F. H. L. Koppens, *Science* **2018**, *360*, 291.
- [15] V. W. Brar, M. C. Sherrott, M. S. Jang, S. Kim, L. Kim, M. Choi, L. A. Sweatlock, H. A. Atwater, *Nat. Commun.* **2015**, *6*, 7032.
- [16] J. Yang, W. Du, Y. S. Su, Y. Fu, S. X. Gong, S. L. He, Y. G. Ma, *Nat. Commun.* **2018**, *9*, 4033.
- [17] S. S. Sunku, G. X. Ni, B. Y. Jiang, H. Yoo, A. Sternbach, A. S. McLeod, T. Stauber, L. Xiong, T. Taniguchi, K. Watanabe, P. Kim, M. M. Fogler, D. N. Basov, *Science* **2018**, *362*, 1153.
- [18] A. J. Giles, S. Y. Dai, I. Vurgaftman, T. H. Man, S. Liu, L. Lindsay, C. T. Ellis, N. Assefa, I. Chatzakos, T. L. Reinecke, J. G. Tischler, M. M. Fogler, J. H. Edgar, D. N. Basov, J. D. Caldwell, *Nat. Mater.* **2018**, *17*, 134.
- [19] S. Dai, Z. Fei, Q. Ma, A. S. Rodin, M. Wagner, A. S. McLeod, M. K. Liu, W. Gannett, W. Regan, K. Watanabe, T. Taniguchi, M. Thiemens, G. Dominguez, A. H. C. Neto, A. Zettl, F. Keilmann, P. Jarillo-Herrero, M. M. Fogler, D. N. Basov, *Science* **2014**, *343*, 1125.
- [20] P. Alonso-Gonzalez, A. Y. Nikitin, Y. Gao, A. Woessner, M. B. Lundeberg, A. Principi, N. Forcellini, W. J. Yan, S. Velez, A. J. Huber, K. Watanabe, T. Taniguchi, F. Casanova, L. E. Hueso, M. Polini, J. Hone, F. H. L. Koppens, R. Hillenbrand, *Nat. Nanotechnol.* **2017**, *12*, 31.
- [21] A. J. Hoffman, L. Alekseyev, S. S. Howard, K. J. Franz, D. Wasserman, V. A. Podolskiy, E. E. Narimanov, D. L. Sivco, C. Gmachl, *Nat. Mater.* **2007**, *6*, 946.
- [22] A. A. High, R. C. Devlin, A. Dibos, M. Polking, D. S. Wild, J. Perczel, N. P. de Leon, M. D. Lukin, H. Park, *Nature* **2015**, *522*, 192.
- [23] Z. W. Liu, H. Lee, Y. Xiong, C. Sun, X. Zhang, *Science* **2007**, *315*, 1686.
- [24] J. S. Gomez-Diaz, A. Alu, *ACS Photonics* **2016**, *3*, 2211.
- [25] C. L. Cortes, W. Newman, S. Molesky, Z. Jacob, *J. Opt.* **2012**, *14*, 063001.
- [26] V. A. Podolskiy, E. E. Narimanov, *Phys. Rev. B* **2005**, *71*, 201101(R).
- [27] A. Falin, Q. R. Cai, E. J. G. Santos, D. Scullion, D. Qian, R. Zhang, Z. Yang, S. M. Huang, K. Watanabe, T. Taniguchi, M. R. Barnett, Y. Chen, R. S. Ruoff, L. H. Li, *Nat. Commun.* **2017**, *8*, 15815.
- [28] S. Dai, Q. Ma, T. Andersen, A. S. McLeod, Z. Fei, M. K. Liu, M. Wagner, K. Watanabe, T. Taniguchi, M. Thiemens, F. Keilmann, P. Jarillo-Herrero, M. M. Fogler, D. N. Basov, *Nat. Commun.* **2015**, *6*, 6963.
- [29] S. Y. Dai, J. M. Quan, G. W. Hu, C. W. Qiu, T. H. Tao, X. Q. Li, A. Alu, *Nano Lett.* **2019**, *19*, 1009.
- [30] P. N. Li, I. Dolado, F. J. Alfaro-Mozaz, F. Casanova, L. E. Hueso, S. Liu, J. H. Edgar, A. Y. Nikitin, S. Velez, R. Hillenbrand, *Science* **2018**, *359*, 892.
- [31] H. Heinzlmann, D. W. Pohl, *Appl. Phys. A* **1994**, *59*, 89.
- [32] C. Maissen, S. Chen, E. Nikulina, A. Goyadinov, R. Hillenbrand, *ACS Photonics* **2019**, *6*, 1279.
- [33] M. Autore, P. N. Li, I. Dolado, F. J. Alfaro-Mozaz, R. Esteban, A. Atxabal, F. Casanova, L. E. Hueso, P. Alonso-Gonzalez, J. Aizpurua, A. Y. Nikitin, S. Velez, R. Hillenbrand, *Light: Sci. Appl.* **2018**, *7*, 17172.
- [34] L. A. Falkovsky, *J. Phys. Conf. Ser.* **2008**, *129*, 012004.
- [35] A. H. Castro Neto, F. Guinea, N. M. R. Peres, K. S. Novoselov, A. K. Geim, *Rev. Mod. Phys.* **2009**, *81*, 109.
- [36] S. Das Sarma, S. Adam, E. H. Hwang, E. Rossi, *Rev. Mod. Phys.* **2011**, *83*, 407.
- [37] M. Jablan, H. Buljan, M. Soljacic, *Phys. Rev. B* **2009**, *80*, 245435.
- [38] Z. Fei, A. S. Rodin, G. O. Andreev, W. Bao, A. S. McLeod, M. Wagner, L. M. Zhang, Z. Zhao, M. Thiemens, G. Dominguez, M. M. Fogler, A. H. Castro Neto, C. N. Lau, F. Keilmann, D. N. Basov, *Nature* **2012**, *487*, 82.
- [39] J. N. Chen, M. Badioli, P. Alonso-Gonzalez, S. Thongrattanasiri, F. Huth, J. Osmond, M. Spasenovic, A. Centeno, A. Pesquera, P. Godignon, A. Z. Elorza, N. Camara, F. J. G. de Abajo, R. Hillenbrand, F. H. L. Koppens, *Nature* **2012**, *487*, 77.
- [40] A. Woessner, M. B. Lundeberg, Y. Gao, A. Principi, P. Alonso-Gonzalez, M. Carrega, K. Watanabe, T. Taniguchi, G. Vignale, M. Polini, J. Hone, R. Hillenbrand, F. H. L. Koppens, *Nat. Mater.* **2015**, *14*, 421.
- [41] G. X. Ni, A. S. McLeod, Z. Sun, L. Wang, L. Xiong, K. W. Post, S. S. Sunku, B. Y. Jiang, J. Hone, C. R. Dean, M. M. Fogler, D. N. Basov, *Nature* **2018**, *557*, 530.
- [42] T. Low, A. S. Rodin, A. Carvalho, Y. J. Jiang, H. Wang, F. N. Xia, A. H. C. Neto, *Phys. Rev. B* **2014**, *90*, 075434.
- [43] S. F. Lan, S. Rodrigues, L. Kang, W. S. Cai, *ACS Photonics* **2016**, *3*, 1176.
- [44] D. J. P. de Sousa, L. V. de Castro, D. R. da Costa, J. M. Pereira, T. Low, *Phys. Rev. B* **2017**, *96*, 155427.
- [45] D. Correas-Serrano, J. S. Gomez-Diaz, A. A. Melcon, A. Alu, *J. Opt.* **2016**, *18*, 104006.
- [46] T. Low, R. Roldan, H. Wang, F. N. Xia, P. Avouris, L. M. Moreno, F. Guinea, *Phys. Rev. Lett.* **2014**, *113*, 106802.
- [47] Z. Z. Liu, K. Aydin, *Nano Lett.* **2016**, *16*, 3457.
- [48] K. Khaliji, A. Fallahi, L. Martin-Moreno, T. Low, *Phys. Rev. B* **2017**, *95*, 201401(R).
- [49] L. K. Li, G. J. Ye, V. Tran, R. X. Fei, G. R. Chen, H. C. Wang, J. Wang, K. Watanabe, T. Taniguchi, L. Yang, X. H. Chen, Y. B. Zhang, *Nat. Nanotechnol.* **2015**, *10*, 608.
- [50] M. A. Huber, F. Mooshammer, M. Plankl, L. Viti, F. Sandner, L. Z. Kastner, T. Frank, J. Fabian, M. S. Vitiello, T. L. Cocker, R. Huber, *Nat. Nanotechnol.* **2017**, *12*, 207.
- [51] A. Woessner, Y. D. Gao, I. Torre, M. B. Lundeberg, C. Tan, K. Watanabe, T. Taniguchi, R. Hillenbrand, J. Hone, M. Polini, F. H. L. Koppens, *Nat. Photonics* **2017**, *11*, 421.
- [52] M. S. Jang, S. Kim, V. W. Brar, S. G. Menabde, H. A. Atwater, *Phys. Rev. Appl.* **2018**, *10*, 054053.
- [53] S. Kim, M. S. Jang, V. W. Brar, Y. Tolstova, K. W. Mauser, H. A. Atwater, *Nat. Commun.* **2016**, *7*, 12323.
- [54] V. W. Brar, M. S. Jang, M. Sherrott, J. J. Lopez, H. A. Atwater, *Nano Lett.* **2013**, *13*, 2541.
- [55] M. S. Jang, V. W. Brar, M. C. Sherrott, J. J. Lopez, L. Kim, S. Kim, M. Choi, H. A. Atwater, *Phys. Rev. B* **2014**, *90*, 165409.
- [56] E. J. C. Dias, F. J. G. de Abajo, *ACS Nano* **2019**, *13*, 5184.
- [57] M. Liu, X. B. Yin, X. Zhang, *Nano Lett.* **2012**, *12*, 1482.
- [58] M. Liu, X. B. Yin, E. Ulin-Avila, B. S. Geng, T. Zentgraf, L. Ju, F. Wang, X. Zhang, *Nature* **2011**, *474*, 64.
- [59] M. Romagnoli, V. Soriano, M. Midrio, F. H. L. Koppens, C. Huyghebaert, D. Neumaier, P. Galli, W. Templ, A. D'Errico, A. C. Ferrari, *Nat. Rev. Mater.* **2018**, *3*, 392.
- [60] V. Soriano, M. Midrio, G. Contestabile, I. Asselberghs, J. Van Campenhout, C. Huyghebaert, I. Goykhman, A. K. Ott, A. C. Ferrari, M. Romagnoli, *Nat. Photonics* **2018**, *12*, 40.
- [61] Y. Yao, M. A. Kats, P. Genevet, N. F. Yu, Y. Song, J. Kong, F. Capasso, *Nano Lett.* **2013**, *13*, 1257.

- [62] Y. Yao, R. Shankar, M. A. Kats, Y. Song, J. Kong, M. Loncar, F. Capasso, *Nano Lett.* **2014**, *14*, 6526.
- [63] M. C. Sherrott, P. W. C. Hon, K. T. Fountaine, J. C. Garcia, S. M. Ponti, V. W. Brar, L. A. Sweatlock, H. A. Atwater, *Nano Lett.* **2017**, *17*, 3027.
- [64] W. L. Gao, J. Shu, K. Reichel, D. V. Nickel, X. W. He, G. Shi, R. Vajtai, P. M. Ajayan, J. Kono, D. M. Mittleman, Q. F. Xu, *Nano Lett.* **2014**, *14*, 1242.
- [65] Y. Yao, M. A. Kats, R. Shankar, Y. Song, J. Kong, M. Loncar, F. Capasso, *Nano Lett.* **2014**, *14*, 214.
- [66] L. Ju, B. S. Geng, J. Horng, C. Girit, M. Martin, Z. Hao, H. A. Bechtel, X. G. Liang, A. Zettl, Y. R. Shen, F. Wang, *Nat. Nanotechnol.* **2011**, *6*, 630.
- [67] H. G. Yan, T. Low, W. J. Zhu, Y. Q. Wu, M. Freitag, X. S. Li, F. Guinea, P. Avouris, F. N. Xia, *Nat. Photonics* **2013**, *7*, 394.
- [68] Z. Y. Fang, Y. M. Wang, A. E. Schather, Z. Liu, P. M. Ajayan, F. J. G. de Abajo, P. Nordlander, X. Zhu, N. J. Halas, *Nano Lett.* **2014**, *14*, 299.
- [69] Z. Y. Fang, S. Thongrattanasiri, A. Schlather, Z. Liu, L. L. Ma, Y. M. Wang, P. M. Ajayan, P. Nordlander, N. J. Halas, F. J. G. de Abajo, *ACS Nano* **2013**, *7*, 2388.
- [70] S. Kim, S. G. Menabde, M. S. Jang, *Adv. Electron. Mater.* **2019**, *5*, 1800940.
- [71] H. G. Yan, X. S. Li, B. Chandra, G. Tulevski, Y. Q. Wu, M. Freitag, W. J. Zhu, P. Avouris, F. N. Xia, *Nat. Nanotechnol.* **2012**, *7*, 330.
- [72] Z. Fei, G. O. Andreev, W. Z. Bao, L. F. M. Zhang, A. S. McLeod, C. Wang, M. K. Stewart, Z. Zhao, G. Dominguez, M. Thiemens, M. M. Fogler, M. J. Tauber, A. H. Castro-Neto, C. N. Lau, F. Keilmann, D. N. Basov, *Nano Lett.* **2011**, *11*, 4701.
- [73] H. G. Yan, Z. Q. Li, X. S. Li, W. J. Zhu, P. Avouris, F. N. Xia, *Nano Lett.* **2012**, *12*, 3766.
- [74] J. Wang, Y. N. Jiang, *Opt. Express* **2017**, *25*, 5206.
- [75] J. P. Nong, W. Wei, W. Wang, G. L. Lan, Z. G. Shang, J. M. Yi, L. L. Tang, *Opt. Express* **2018**, *26*, 1633.
- [76] N. Liu, M. Mesch, T. Weiss, M. Hentschel, H. Giessen, *Nano Lett.* **2010**, *10*, 2342.
- [77] C. H. Wu, B. Neuner, G. Shvets, J. John, A. Milder, B. Zollars, S. Savoy, *Phys. Rev. B* **2011**, *84*, 075102.
- [78] A. Tittl, A. K. U. Michel, M. Schaferling, X. H. Yin, B. Gholipour, L. Cui, M. Wuttig, T. Taubner, F. Neubrech, H. Giessen, *Adv. Mater.* **2015**, *27*, 4597.
- [79] D. Rodrigo, A. Tittl, O. Limaj, F. J. G. de Abajo, V. Pruneri, H. Altug, *Light: Sci. Appl.* **2017**, *6*, e16277.
- [80] S. Thongrattanasiri, F. H. L. Koppens, F. J. G. de Abajo, *Phys. Rev. Lett.* **2012**, *108*, 047401.
- [81] J. A. Gerber, S. Berweger, B. T. O'Callahan, M. B. Raschke, *Phys. Rev. Lett.* **2014**, *113*, 055502.
- [82] A. Pirkle, J. Chan, A. Venugopal, D. Hinojos, C. W. Magnuson, S. McDonnell, L. Colombo, E. M. Vogel, R. S. Ruoff, R. M. Wallace, *Appl. Phys. Lett.* **2011**, *99*, 122108.
- [83] J. Chan, A. Venugopal, A. Pirkle, S. McDonnell, D. Hinojos, C. W. Magnuson, R. S. Ruoff, L. Colombo, R. M. Wallace, E. M. Vogel, *ACS Nano* **2012**, *6*, 3224.
- [84] A. Venugopal, J. Chan, X. S. Li, C. W. Magnuson, W. P. Kirk, L. Colombo, R. S. Ruoff, E. M. Vogel, *J. Appl. Phys.* **2011**, *109*, 104511.
- [85] Z. Fei, M. D. Goldflam, J. S. Wu, S. Dai, M. Wagner, A. S. McLeod, M. K. Liu, K. W. Post, S. Zhu, G. C. A. M. Janssen, M. M. Fogler, D. N. Basov, *Nano Lett.* **2015**, *15*, 8271.
- [86] A. Novitsky, A. M. Ivinskaya, M. Zalkovskij, R. Malureanu, P. U. Jepsen, A. V. Lavrinenko, *J. Appl. Phys.* **2012**, *112*, 074318.
- [87] M. A. Seo, H. R. Park, S. M. Koo, D. J. Park, J. H. Kang, O. K. Suwal, S. S. Choi, P. C. M. Planken, G. S. Park, N. K. Park, Q. H. Park, D. S. Kim, *Nat. Photonics* **2009**, *3*, 152.
- [88] T. W. Ebbesen, H. J. Lezec, H. F. Ghaemi, T. Thio, P. A. Wolff, *Nature* **1998**, *391*, 667.
- [89] L. Martin-Moreno, F. J. Garcia-Vidal, H. J. Lezec, K. M. Pellerin, T. Thio, J. B. Pendry, T. W. Ebbesen, *Phys. Rev. Lett.* **2001**, *86*, 1114.
- [90] J. A. Porto, F. J. Garcia-Vidal, J. B. Pendry, *Phys. Rev. Lett.* **1999**, *83*, 2845.
- [91] P. Q. Liu, I. J. Luxmoore, S. A. Mikhailov, N. A. Savostianova, F. Valmorra, J. Faist, G. R. Nash, *Nat. Commun.* **2015**, *6*, 8969.
- [92] D. Rodrigo, O. Limaj, D. Janner, D. Etezadi, F. J. G. de Abajo, V. Pruneri, H. Altug, *Science* **2015**, *349*, 165.
- [93] A. Marini, I. Silveiro, F. J. G. de Abajo, *ACS Photonics* **2015**, *2*, 876.
- [94] M. Osawa, *Top. Appl. Phys.* **2001**, *81*, 163.
- [95] R. Kellner, B. Mizsaikoff, M. Jakusch, H. D. Wanzenbock, N. Weissenbacher, *Appl. Spectrosc.* **1997**, *51*, 495.
- [96] F. Neubrech, A. Pucci, T. W. Cornelius, S. Karim, A. Garcia-Etxarri, J. Aizpurua, *Phys. Rev. Lett.* **2008**, *101*, 157403.
- [97] A. J. Giles, S. Y. Dai, O. J. Glembocki, A. V. Kretinin, Z. Y. Sun, C. T. Ellis, J. G. Tischler, T. Taniguchi, K. Watanabe, M. M. Fogler, K. S. Novoselov, D. N. Basov, J. D. Caldwell, *Nano Lett.* **2016**, *16*, 3858.
- [98] F. J. Alfaro-Mozaz, P. Alonso-Gonzalez, S. Velez, I. Dolado, M. Autore, S. Mastel, F. Casanova, L. E. Hueso, P. Li, A. Y. Nikitin, R. Hillenbrand, *Nat. Commun.* **2017**, *8*, 15624.
- [99] J. D. Caldwell, A. V. Kretinin, Y. G. Chen, V. Giannini, M. M. Fogler, Y. Francescato, C. T. Ellis, J. G. Tischler, C. R. Woods, A. J. Giles, M. Hong, K. Watanabe, T. Taniguchi, S. A. Maier, K. S. Novoselov, *Nat. Commun.* **2014**, *5*, 5221.
- [100] V. W. Brar, M. S. Jang, M. Sherrott, S. Kim, J. J. Lopez, L. B. Kim, M. Choi, H. Atwater, *Nano Lett.* **2014**, *14*, 3876.
- [101] H. Hu, X. X. Yang, F. Zhai, D. B. Hu, R. N. Liu, K. H. Liu, Z. P. Sun, Q. Dai, *Nat. Commun.* **2016**, *7*, 12334.
- [102] H. Hu, X. X. Yang, X. D. Guo, K. Khaliji, S. R. Biswas, F. J. G. de Abajo, T. Low, Z. P. Sun, Q. Dai, *Nat. Commun.* **2019**, *10*, 1131.
- [103] Y. L. Li, H. G. Yan, D. B. Farmer, X. Meng, W. J. Zhu, R. M. Osgood, T. F. Heinz, P. Avouris, *Nano Lett.* **2014**, *14*, 1573.
- [104] D. B. Farmer, P. Avouris, Y. L. Li, T. F. Heinz, S. J. Han, *ACS Photonics* **2016**, *3*, 553.
- [105] M. Osawa, M. Ikeda, *J. Phys. Chem.* **1991**, *95*, 9914.
- [106] M. B. Lundberg, Y. D. Gao, R. Asgari, C. Tan, B. Van Duppen, M. Autore, P. Alonso-Gonzalez, A. Woessner, K. Watanabe, T. Taniguchi, R. Hillenbrand, J. Hone, M. Polini, F. H. L. Koppens, *Science* **2017**, *357*, 187.
- [107] I. H. Lee, L. Martin-Moreno, D. A. Mohr, K. Khaliji, T. Low, S. H. Oh, *ACS Photonics* **2018**, *5*, 2208.
- [108] I. H. Lee, D. Yoo, P. Avouris, T. Low, S. H. Oh, *Nat. Nanotechnol.* **2019**, *14*, 313.
- [109] W. Li, S. H. Fan, *Opt. Express* **2018**, *26*, 15995.
- [110] L. X. Ge, Y. P. Cang, K. Gong, L. H. Zhou, D. Q. Yu, Y. S. Luo, *AIP Adv.* **2018**, *8*, 085321.
- [111] V. Fernandez-Hurtado, A. I. Fernandez-Dominguez, J. Feist, F. J. Garcia-Vidal, J. C. Cuevas, *ACS Photonics* **2018**, *5*, 3082.
- [112] X. L. Liu, Z. M. Zhang, *Appl. Phys. Lett.* **2015**, *107*, 143114.
- [113] T. Inoue, M. De Zoysa, T. Asano, S. Noda, *Nat. Mater.* **2014**, *13*, 928.
- [114] J. C. Cuevas, F. J. Garcia-Vidal, *ACS Photonics* **2018**, *5*, 3896.
- [115] O. Ilic, M. Jablan, J. D. Joannopoulos, I. Celanovic, H. Buljan, M. Soljacic, *Phys. Rev. B* **2012**, *85*, 155422.
- [116] V. B. Svetovoy, P. J. van Zwol, J. Chevrier, *Phys. Rev. B* **2012**, *85*, 155418.
- [117] P. J. van Zwol, S. Thiele, C. Berger, W. A. de Heer, J. Chevrier, *Phys. Rev. Lett.* **2012**, *109*, 264301.
- [118] Y. Zhang, H. L. Yi, H. P. Tan, *ACS Photonics* **2018**, *5*, 3739.
- [119] Y. Guo, C. L. Cortes, S. Molesky, Z. Jacob, *Appl. Phys. Lett.* **2012**, *101*, 131106.
- [120] R. W. Yu, A. Manjavacas, F. J. G. de Abajo, *Nat. Commun.* **2017**, *8*, 2.

- [121] V. Fernandez-Hurtado, A. I. Fernandez-Dominguez, J. Feist, F. J. Garcia-Vidal, J. C. Cuevas, *Phys. Rev. B* **2018**, *97*, 045408.
- [122] D. Thompson, L. X. Zhu, R. Mittapally, S. Sadat, Z. Xing, P. McArdle, M. M. Qazilbash, P. Reddy, E. Meyhofer, *Nature* **2018**, *561*, 216.
- [123] J. C. W. Song, N. M. Gabor, *Nat. Nanotechnol.* **2018**, *13*, 986.
- [124] S. Dai, Q. Ma, M. K. Liu, T. Andersen, Z. Fei, M. D. Goldflam, M. Wagner, K. Watanabe, T. Taniguchi, M. Thiemens, F. Keilmann, G. C. A. M. Janssen, S. E. Zhu, P. Jarillo-Herrero, M. M. Fogler, D. N. Basov, *Nat. Nanotechnol.* **2015**, *10*, 682.
- [125] M. Settnes, J. R. M. Saavedra, K. S. Thygesen, A. P. Jauho, F. J. G. de Abajo, N. A. Mortensen, *ACS Photonics* **2017**, *4*, 2908.
- [126] K. Chaudhary, M. Tamagnone, M. Rezaee, D. K. Bediako, A. Ambrosio, P. Kim, F. Capasso, *Sci. Adv.* **2019**, *5*, eaau7171.
- [127] C. Forsythe, X. D. Zhou, K. Watanabe, T. Taniguchi, A. Pasupathy, P. Moon, M. Koshino, P. Kim, C. R. Dean, *Nat. Nanotechnol.* **2018**, *13*, 566.
- [128] M. Takamura, N. Kumada, S. N. Wang, K. Kumakura, Y. Taniyasu, *ACS Photonics* **2019**, *6*, 947.
- [129] G. X. Ni, H. Wang, J. S. Wu, Z. Fei, M. D. Goldflam, F. Keilmann, B. Ozylmaz, A. H. Castro Neto, X. M. Xie, M. M. Fogler, D. N. Basov, *Nat. Mater.* **2015**, *14*, 1217.
- [130] A. Tomadin, M. Polini, J. Jung, *Phys. Rev. B* **2019**, *99*, 035432.
- [131] T. Stauber, H. Kohler, *Nano Lett.* **2016**, *16*, 6844.
- [132] L. Wang, I. Meric, P. Y. Huang, Q. Gao, Y. Gao, H. Tran, T. Taniguchi, K. Watanabe, L. M. Campos, D. A. Muller, J. Guo, P. Kim, J. Hone, K. L. Shepard, C. R. Dean, *Science* **2013**, *342*, 614.
- [133] R. Frisenda, E. Navarro-Moratalla, P. Gant, D. P. De Lara, P. Jarillo-Herrero, R. V. Gorbachev, A. Castellanos-Gomez, *Chem. Soc. Rev.* **2018**, *47*, 53.
- [134] L. Banszerus, M. Schmitz, S. Engels, J. Dauber, M. Oellers, F. Haupt, K. Watanabe, T. Taniguchi, B. Beschoten, C. Stampfer, *Sci. Adv.* **2015**, *1*, e1500222.
- [135] A. K. Geim, I. V. Grigorieva, *Nature* **2013**, *499*, 419.
- [136] S. G. Menabde, D. R. Mason, E. E. Kornev, C. Lee, N. Park, *Sci. Rep.* **2016**, *6*, 21523.
- [137] Z. Fei, E. G. Iwinski, G. X. Ni, L. M. Zhang, W. Bao, A. S. Rodin, Y. Lee, M. Wagner, M. K. Liu, S. Dai, M. D. Goldflam, M. Thiemens, F. Keilmann, C. N. Lau, A. H. Castro-Neto, M. M. Fogler, D. N. Basov, *Nano Lett.* **2015**, *15*, 4973.
- [138] K. Yu, N. V. Luan, T. Kim, J. Jeon, J. Kim, P. Moon, Y. H. Lee, E. J. Choi, *Phys. Rev. B* **2019**, *99*, 241405(R).
- [139] J. M. B. L. dos Santos, N. M. R. Peres, A. H. Castro, *Phys. Rev. Lett.* **2007**, *99*, 256802.
- [140] V. Carozo, C. M. Almeida, B. Fragneaud, P. M. Bede, M. V. O. Moutinho, J. Ribeiro-Soares, N. F. Andrade, A. G. Souza, M. J. S. Matos, B. Wang, M. Terrones, R. B. Capaz, A. Jorio, C. A. Achete, L. G. Cancado, *Phys. Rev. B* **2013**, *88*, 085401.
- [141] F. Hu, S. R. Das, Y. Luan, T. F. Chung, Y. P. Chen, Z. Fei, *Phys. Rev. Lett.* **2017**, *119*, 247402.
- [142] H. C. Po, L. J. Zou, A. Vishwanath, T. Senthil, *Phys. Rev. X* **2018**, *8*, 031089.
- [143] H. Yoo, R. Engelke, S. Carr, S. A. Fang, K. Zhang, P. Cazeaux, S. H. Sung, R. Hoyden, A. W. Tsen, T. Taniguchi, K. Watanabe, G. C. Yi, M. Kim, M. Luskun, E. B. Tadmor, E. Kaxiras, P. Kim, *Nat. Mater.* **2019**, *18*, 448.
- [144] B. Y. Jiang, G. X. Ni, Z. Addison, J. K. Shi, X. M. Liu, S. Y. F. Zhao, P. Kim, E. J. Mele, D. N. Basov, M. M. Fogler, *Nano Lett.* **2017**, *17*, 7080.
- [145] S. Huang, K. Kim, D. K. Efimkin, T. Lovorn, T. Taniguchi, K. Watanabe, A. H. MacDonald, E. Tutuc, B. J. LeRoy, *Phys. Rev. Lett.* **2018**, *121*, 037702.
- [146] N. Y. Kim, H. Y. Jeong, J. H. Kim, G. Kim, H. S. Shin, Z. Lee, *ACS Nano* **2017**, *11*, 7084.
- [147] J. Jung, E. Laksono, A. M. DaSilva, A. H. MacDonald, M. Mucha-Kruczynski, S. Adam, *Phys. Rev. B* **2017**, *96*, 085442.
- [148] D. F. Jin, T. Christensen, M. Soljacic, N. X. Fang, L. Lu, X. Zhang, *Phys. Rev. Lett.* **2017**, *118*, 245301.
- [149] D. Pan, R. Yu, H. X. Xu, F. J. G. de Abajo, *Nat. Commun.* **2017**, *8*, 1243.
- [150] T. Ozawa, H. M. Price, A. Amo, N. Goldman, M. Hafezi, L. Lu, M. C. Rechtsman, D. Schuster, J. Simon, O. Zilberberg, I. Carusotto, *Rev. Mod. Phys.* **2019**, *91*, 015006.
- [151] P. Di Pietro, M. Ortolani, O. Limaj, A. Di Gaspere, V. Giliberti, F. Giorgianni, M. Brahlek, N. Bansal, N. Koirala, S. Oh, P. Calvani, S. Lupi, *Nat. Nanotechnol.* **2013**, *8*, 556.
- [152] M. C. Sherrott, W. S. Whitney, D. Jariwala, S. Biswas, C. M. Went, J. Wong, G. R. Rossman, H. A. Atwater, *Nano Lett.* **2019**, *19*, 269.
- [153] A. Majumdar, J. Kim, J. Vuckovic, F. Wang, *Nano Lett.* **2013**, *13*, 515.
- [154] R. J. Shiu, Y. D. Gao, C. Tan, C. Peng, J. B. Zheng, D. K. Efetov, Y. D. Kim, J. Hone, D. Englund, *Nat. Commun.* **2019**, *10*, 109.
- [155] N. Dabidian, I. Kholmanov, A. B. Khanikaev, K. Tatar, S. Trendafilov, S. H. Mousavi, C. Magnuson, R. S. Ruoff, G. Shvets, *ACS Photonics* **2015**, *2*, 216.
- [156] K. Tran, G. Moody, F. C. Wu, X. B. Lu, J. Choi, K. Kim, A. Rai, D. A. Sanchez, J. M. Quan, A. Singh, J. Embley, A. Zepeda, M. Campbell, T. Autry, T. Taniguchi, K. Watanabe, N. S. Lu, S. K. Banerjee, K. L. Silverman, S. Kim, E. Tutuc, L. Yang, A. H. MacDonald, X. Q. Li, *Nature* **2019**, *567*, 71.
- [157] F. C. Wu, T. Lovorn, E. Tutuc, I. Martin, A. H. MacDonald, *Phys. Rev. Lett.* **2019**, *122*, 086402.
- [158] D. A. Bandurin, I. Torre, R. K. Kumar, M. Ben Shalom, A. Tomadin, A. Principi, G. H. Auton, E. Khestanova, K. S. Novoselov, I. V. Grigorieva, L. A. Ponomarenko, A. K. Geim, M. Polini, *Science* **2016**, *351*, 1055.
- [159] K. S. Novoselov, D. Jiang, F. Schedin, T. J. Booth, V. V. Khotkevich, S. V. Morozov, A. K. Geim, *Proc. Natl. Acad. Sci. USA* **2005**, *102*, 10451.
- [160] K. Eda, *J. Solid State Chem.* **1991**, *95*, 64.
- [161] S. Narita, S. Terada, S. Mori, K. Muro, Y. Akahama, S. Endo, *J. Phys. Soc. Jpn.* **1983**, *52*, 3544.
- [162] J. M. Pereira, M. I. Katsnelson, *Phys. Rev. B* **2015**, *92*, 075437.